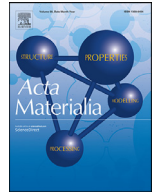




ELSEVIER

Contents lists available at ScienceDirect

Acta Materialia

journal homepage: [www.elsevier.com/locate/actamat](http://www.elsevier.com/locate/actamat)

# Micromechanical behavior of multilayered Ti/Nb composites processed by accumulative roll bonding: An *in-situ* synchrotron X-ray diffraction investigation

S. Jiang<sup>a</sup>, R. Lin Peng<sup>b</sup>, Z. Hegedűs<sup>c</sup>, T. Gnäupel-Herold<sup>d</sup>, J.J. Moverare<sup>b</sup>, U. Lienert<sup>c</sup>, F. Fang<sup>e</sup>, X. Zhao<sup>a</sup>, L. Zuo<sup>a</sup>, N. Jia<sup>a,\*</sup>

<sup>a</sup> Key Laboratory for Anisotropy and Texture of Materials (Ministry of Education), School of Material Science and Engineering, Northeastern University, Shenyang 110819, China

<sup>b</sup> Division of Engineering Materials, Department of Management and Engineering, Linköping University, Linköping, SE-58183, Sweden

<sup>c</sup> Deutsches Elektronen-Synchrotron (DESY), Hamburg 22607, Germany

<sup>d</sup> NIST Center for Neutron Research, Gaithersburg, MD 20899-8562, USA

<sup>e</sup> The State Key Lab of Rolling & Automation, Northeastern University, Shenyang 110819, China

## ARTICLE INFO

### Article history:

Received 3 July 2020

Revised 6 November 2020

Accepted 3 December 2020

Available online 9 December 2020

### Keywords:

Ti/Nb multilayers

Micromechanical behavior

High-energy X-ray diffraction

Lattice strain

Load partitioning

## ABSTRACT

Heterophase interfaces play a crucial role in deformation microstructures and thus govern mechanical properties of multilayered composites. Here, we fabricated Ti/Nb multilayers by accumulative roll bonding (ARB) where shear bands became predominant with increasing rolling cycles. To explore correlation between micromechanical behavior and mechanical properties of the composites with various lamellar morphologies, *in-situ* high-energy X-ray diffraction tensile tests were performed. The results quantitatively reveal that the rapid strengthening of the composites with increasing ARB cycles mainly originates from the Nb layers strengthened by dislocations, grain boundaries and heterophase interfaces, and the {211} grains mostly contribute to the global strain hardening. The softer Ti grains also extend global strain hardening to a wide range and postpone necking. Furthermore, complete stress state analysis show that in the presence of extensive shear bands, significant load partitioning between the neighboring metals leads to triaxial stresses in each constituent and dislocations tend to slip along the shear direction. This promotes dislocation multiplication and motion, which is conducive to overall strength enhancement while maintaining a satisfactory ductility. These findings elucidate the effect of strong constraints of the interfaces on mechanical properties, which provides a fundamental understanding of load partitioning and strengthening mechanisms of the multilayers processed by multiple ARB cycles.

© 2020 Acta Materialia Inc. Published by Elsevier Ltd. All rights reserved.

## 1. Introduction

Both strength and ductility are essential for metallic materials in engineering application. However, they normally contradict each other, which is known as the strength-ductility trade-off represented by the banana-shaped curve [1,2]. Severe plastic deformation (SPD) [3,4] opens up possibilities for obtaining ultra-strong materials without compositional complexity. Unfortunately, this is accompanied with the significant loss of ductility and the saturated strength at the utmost deformation [5]. In the past two decades, numerous materials with heterogeneous structures, e.g. multilayered, bimodal and gradient structures, have been developed for pursuing outstanding mechanical properties [6–12]. Espe-

cially, multilayered composites composed of dissimilar metals have attracted great attention owing to their significant constraint effect exerted by the heterophase interfaces [7,8] as well as good plasticity mediated by those interfaces [13]. Accumulative roll bonding (ARB) [14] which is low-cost and suitable for industrial processing has been widely applied for fabricating bulk composites, such as copper/bronze [8], Al-laminates [15], Cu/Nb [16,17], Cu/Ta [18], Fe/Ni [19], Zr/Nb [20–22], Mg/Nb [23] and twinning-induced plasticity (TWIP)/low-carbon (LC) steel sheets [24].

For a multilayered composite under loading, the stress partitioning between the constituent metals directly affects mechanical properties of the bulk material. By performing neutron diffraction measurements, three-stage stress partitioning has been found in multilayered Ti/Al [6] and steel sheets [25,26] under uniaxial tensile testing. At stage I (elastic regime), both metals deform elastically and the stiffer metal layers bear the larger stress. This stress

\* Corresponding author.

E-mail address: [jian@atm.neu.edu.cn](mailto:jian@atm.neu.edu.cn) (N. Jia).

partitioning results in an internal stress accumulated at the heterophase interfaces. At stage II (elastic-plastic regime) where the soft layers start to deform plastically and the stiff ones still deform elastically, internal stress at the heterophase interfaces increases with deformation. The strong synergetic interaction between the constituent metals may lead to a biaxial stress state [27]. When the applied stress is elevated further and exceeds yield points of both metals (stage III), deformation compatibility between the constituents is improved and internal stress is weakened. In addition, multilayered composites usually show the higher flow stress than that estimated by using the mixture rule [24], which is attributed to the specific mechanism operated at the heterophase interfaces, i.e. back-stress strengthening. During plastic deformation, back stress and additional geometrically necessary dislocations (GNDs) are generated to relieve the significant deformation incompatibility across the interfaces [8]. Accordingly, hetero-deformation induced (HDI) strengthening and work hardening may lead to a superior combination of strength and ductility [11]. On the other hand, ductility of such materials tends to be limited by the onset of the banded structures, i.e. slip bands and shear bands (SBs), where intense plastic strain has been localized during deformation [7,22,28–30]. Formation of the bands depends on the interactions between dislocations and heterophase interfaces. To be explicit, dislocation transmission across the interfaces results in the formation of crystallographic bands, i.e. slip bands, whereas the resistance to dislocation transmission across the interfaces leads to the formation of non-crystallographic shear bands [30]. Moreover, for a co-deformed multilayered composite, deformation mechanisms in each constituent can be modified under the effect of interfaces [21,23,29], and some unexpected slip and twinning systems are activated [7,30]. The initial thickness of each single layer is the key parameter determining the mechanical properties of bulk composites, as deformation behaviors of the constituents can be strongly size-dependent [16,31,32]. This size-dependence relies on the interaction between dislocations and heterophase interfaces/grain boundaries [33]. In a composite with coarse layers (thickness  $h \sim 10^{-3} - 10^{-5}$  m), strength depends on the grain size within individual layers [15]. For the sub-micron and nanolayered composites, three mechanistic regimes have been proposed: i) When the layer thickness is in the micron scale ( $h > 100$  nm), dislocation pile-up based Hall-Petch law is applicable; ii) As the layer thickness is reduced to a few tens of nanometers, the confined layer slip (CLS) that involves propagation of individual dislocation loops parallel to heterophase interfaces dominates; iii) As the layer thickness is only a few nanometers ( $h < 10$  nm), dislocation transmission across heterophase interfaces is the main mechanism, and the saturation in strength/hardness appears [34,35].

So far, micromechanical behavior of multilayered composites has been extensively studied by means of electron microscopy [30,31,35–40] and numerical modeling [21,23,24,41–43]. However, if shear banding already predominates a multilayered structure or the bands develop with deformation, how the heterophase interfaces mediate strain/stress partitioning between the constituent metals and thus govern mechanical properties of the bulk material is still unknown. To postpone mechanical instabilities caused by the initiation of SBs and thus enhance ductility, it is imperative to study the micromechanical behavior of the multilayers. With the help of neutron diffraction and high-energy X-ray diffraction (HEXRD) techniques, these can be revealed by measuring lattice strains of various crystallographic planes. However, previous investigations on load partitioning of multilayered composites have been conducted mostly with neutrons. Due to the limited detector banks, lattice strains were measured only in two directions, i.e. the loading and the transverse directions, based on which the micromechanical behavior was inferred [6,25,26]. As a triaxial stress

state is expected from the layer-to-layer interactions which will become more complicated in the presence of extensive shear bands, analysis of the complete stress state is important for understanding the role of microstructure in such materials.

In this work, we employed the *in-situ* HEXRD technique to investigate the distribution of lattice strains, load partitioning and complete stress state of individual metals within the ARB processed Ti/Nb multilayers under deformation. For the first time, the evolution of complete stress state under the strong constraints of heterophase interfaces was obtained. By analyzing load partitioning between the constituent metals and among the various lattice reflections of the composites with two typical lamellar morphologies, i.e. those with and without shear bands, the micromechanical behaviors that contribute to mechanical properties of the bulk composites were clarified. The present results not only provide the fundamental understanding of the deformation behaviors affected by heterophase interfaces, but also shed light on the design of advanced multilayers with superior strength and ductility synergy.

## 2. Materials and methods

### 2.1. Composites fabrication

Multilayered Ti/Nb composites were fabricated via the ARB technique. The starting metals were 1 mm thick sheets of commercial pure titanium (CP-Ti, 99.8 wt.% purity) and pure niobium (99.9 wt.% purity), both of which were at the fully recrystallized state (Fig. S1, Supplementary material). First, surface cleaning treatment consisting of a 5 min ultrasonic acetone bath and the subsequent wire brushing was performed to remove oxide layer and foster bonding. Then, four Ti and three Nb sheets were stacked alternately and heated in a preheated furnace at a temperature of 300 °C for 20 min. Subsequently, they were roll-bonded by the un-heated rolls with a nominal thickness reduction of 65% by one single pass followed by air cooling. Rolling was performed using a two-high rolling mill with two 400 mm diameter rolls and a rolling speed of  $1 \text{ m} \cdot \text{s}^{-1}$ . This procedure produced a sandwiched composite, i.e. the N1 composite. Annealing was then performed at 575 °C for 1 hour in a vacuum furnace prior to the subsequent ARB processing, in order to ensure a good bonding and also to reduce the difference in strength between the different metals. As Ti and Nb are immiscible at that temperature [44], intermixing at the heterophase interfaces is not expected. The bonded sheet was cut into several pieces, and then surface cleaned, restacked and rolled. This produced the N2 composite. Hereafter, the ARB process was repeated up to 8 cycles. The rolling direction was kept constant throughout the ARB processing. It should be mentioned that the intermediate annealing treatment was conducted after every roll bonding cycle. Three orthonormal directions, i.e. rolling direction (RD), transverse direction (TD) and normal direction (ND) of the bulk composites are used to define the sample coordinate. Table 1 shows the designed number of metal layers, the nominal layer thickness  $h$ , and the equivalent true strain  $e$  [45] associated with each ARB processed composites, where the nominal layer thickness is defined as the total thickness of the composite divided by the number of the constituent layers. All samples investigated in the present work are in the as-ARBed condition, i.e. the composites undergone intermediate heat treatments are not considered.

### 2.2. Microstructural characterization and tensile test

Microstructures of the ARB processed composites were first studied with a JEOL JSM-7001F scanning electron microscope (SEM) to reveal the lamellar morphologies. The detailed microstructures of the composite after the eighth ARB cycle were studied using a Tecnai F20 transmission electron microscope

**Table 1**

The number of metal layers, nominal layer thickness  $h$  and total strain  $e$  for the composites fabricated by the ARB processing.

Composites	Number of layers	Nominal layer thickness ( $h$ , $\mu\text{m}$ )	Equivalent true strain ( $e$ )
N1	7	368	1.15
N2	14	130.5	2.35
N3	42	47.9	3.51
N4	126	15.1	4.84
N5	378	5	6.12
N6	1134	1.6	7.43
N7	3402	0.57	8.63
N8	6802	0.245	9.60

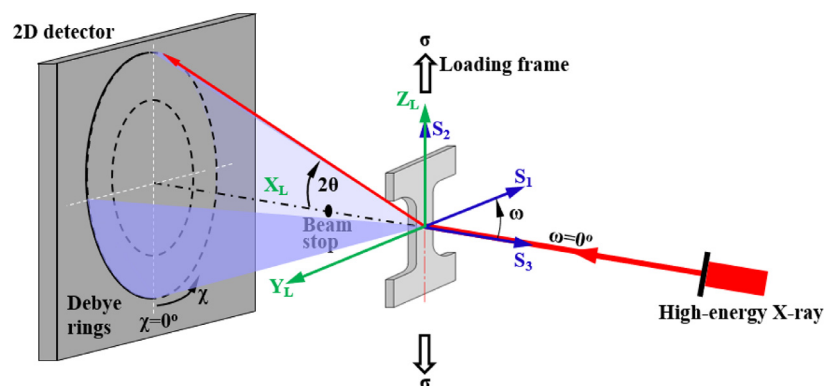


**Fig. 1.** Schematic showing the experimental set-up of *in-situ* HEXRD measurements.  $X_L$ - $Y_L$ - $Z_L$ : laboratory coordinates defining the geometry of diffraction cones.  $S_1$ - $S_2$ - $S_3$ : sample coordinates.

(TEM). The foils were extracted from the ND-RD plane using FEI Helios NanoLab 600i focused ion beam (FIB). The bulk crystallographic textures for Ti and Nb within the composites were measured by neutron diffraction, using the Residual Stress Diffractometer (BT-8) at the Center for Neutron Research at National Institute of Standards and Technology (NIST). The raw data of the  $\{10\bar{1}0\}$ ,  $\{10\bar{1}1\}$ ,  $\{11\bar{2}2\}$  and  $\{20\bar{2}1\}$  pole figures of Ti and the  $\{110\}$ ,  $\{200\}$  and  $\{211\}$  pole figures of Nb were processed using the MTEX algorithm [46] to obtain the orientation distribution functions (ODFs). To reveal mechanical properties of the ARB processed composites, uniaxial tensile tests with the loading direction (LD) parallel to RD were carried out at room temperature using a Shimadzu AG-Xplus machine. Flat tensile specimens with the gauge length of 13 mm, width of 3 mm and thickness in the range of 1.6–2 mm were used. The strain rate was  $10^{-3} \text{ s}^{-1}$ . To ensure the repeatability of the tensile properties, three specimens were tested for each composite.

### 2.3. In-situ HEXRD measurements

Lattice strain distribution and evolution of the multilayered composites under uniaxial tensile loading were studied using the Swedish Materials Science beamline P21 of the PETRA III synchrotron facility at DESY. Fig. 1 shows the geometry of *in-situ* diffraction measurements, sample coordinates ( $S_1$ - $S_2$ - $S_3$ ) and laboratory coordinates ( $X_L$ - $Y_L$ - $Z_L$ ). The photon energy was 67 keV, corresponding to a wavelength of 0.18504 Å. The diffraction rings of Ti and Nb were measured in transmission mode on a 2D Varex XRD 4343CT detector ( $2880 \times 2880$  pixels, with pixel size of  $150 \mu\text{m}$ ) with a sample-to-detector distance of 1 m. Different exposure time in the range of 0.3–0.8 s was used to obtain a single diffraction image according to the maximum intensity. At each loading point, 20 frames of diffraction patterns were recorded in order to obtain high quality diffraction data, which made the subsequent refinements and analysis feasible. In the *in-situ* tensile experiments, flat dog-bone specimens machined from the as-ARBed materials were used, with LD parallel to RD and the incident X-ray beam par-

allel to ND, respectively. The loading frame was controlled in a step-stress-controlled manner in the elastic regime and in a step-displacement-controlled manner in the plastic regime with a strain rate of  $10^{-3} \text{ s}^{-1}$ . After holding for 300 s when the stress was relaxed to a stable state at every loading step, the diffraction patterns and optical images of sample surface were captured for estimating lattice strain and applied true strain. In addition, the loading frame was rotated around LD from  $90^\circ$  to  $150^\circ$  and the diffraction patterns were collected at an interval of  $\omega=5^\circ$ . With the fixed sample-to-detector distance, the measurements at  $\omega=90^\circ$ ,  $120^\circ$  and  $150^\circ$  were used for deriving the complete strain/stress tensors.

### 2.4. Diffraction profiles analysis

For the HEXRD analysis, pyFAI [47], which is a Python library for high performance azimuthal integration, was used to dissect the complete 2D Debye rings into 36 linear intensity versus diffraction angle profiles with an azimuth range of  $\pm 5^\circ$ . Four diffraction peaks of Ti ( $\{10\bar{1}0\}$ ,  $\{10\bar{1}1\}$ ,  $\{11\bar{2}0\}$ ,  $\{11\bar{2}2\}$ ) and three peaks of Nb ( $\{200\}$ ,  $\{211\}$ ,  $\{310\}$ ) were fitted with a Pseudo-Voigt function, and the error in peak position was extremely low ( $<0.0005^\circ$ ). The lattice strains of the constituent metals were estimated from the change in the interplanar spacing (d-spacing) with respect to the state without loading:

$$\varepsilon_{hkl} = \frac{d_{hkl} - d_{hkl}^0}{d_{hkl}^0} \quad (1)$$

where  $d_{hkl}$  and  $d_{hkl}^0$  denote the interplanar spacing of the  $\{hkl\}$  crystallographic planes with and without external loading, respectively. Then, the complete strain tensor was estimated using the coordinate transformation and the least square method. The generalized Hooke's law was used for calculating the stress tensor of respective metals/orientations under different loading stages. Considering the small errors of peak position, the error of the calculated stress is estimated to be less than 6 MPa. Here, the complete stress tensor is expressed in sample coordinates ( $S_1$ - $S_2$ - $S_3$ ), with

the main diagonal components along TD ( $\sigma_{11}$ ), RD ( $\sigma_{22}$ ) and ND ( $\sigma_{33}$ ). The relevant diffraction elastic constants (DECs) were calculated using the ISODEF software [48], as shown in Table S1 (Supplementary material).

Dislocation density was estimated with the modified Williamson-Hall (W-H) method. Dislocation density ( $\rho$ ) and coherent domain size ( $D$ ) can be determined by tracing the change in slope and intercept of the modified W-H plot [49] obtained from the HEXRD measurements, i.e.:

$$\Delta K_{\text{hkl}} \cong \frac{0.9}{D} + \left( \frac{\pi M_d^2 b^2}{2} \right)^{1/2} \rho^{1/2} \left( K_{\text{hkl}} \bar{C}_{\text{hkl}}^{1/2} \right) + O(K_{\text{hkl}}^2 \bar{C}_{\text{hkl}}) \quad (2)$$

where  $K=2\sin\theta/\lambda$  and  $\Delta K=2\cos\theta(\Delta\theta)/\lambda$ .  $\Delta\theta$  is the full width at half maximum (FWHM) of the diffraction peak,  $\theta$  and  $\lambda$  are the diffraction angle and the wavelength of X-ray.  $b$  is the Burgers vector,  $M_d$  is a parameter depending on the effective outer cut-off radius of dislocations and  $\bar{C}$  is the average dislocation contrast factor (Table S2, Supplementary material), respectively. All the parameters needed for the calculations are summarized in Table S3 (Supplementary material). It should be noted that the realistic FWHM should be calibrated by extracting the instrumental broadening from the measured value. Here, the instrumental contribution was determined using a  $\text{LaB}_6$  powder reference. Moreover, due to the elastic anisotropy and the orientation-dependent deformation behavior, especially after the activation of multiple slip systems in the both hcp and bcc constituents, dislocation densities of individual metals are deduced from the elaborately fitted diffraction profiles with the convolutional multiple whole profile (CMWP) method [50,51]. To ensure good statistics, an azimuth angle of  $\pm 15^\circ$  along the Debye ring around the transverse direction, i.e. the axis of  $\chi=90^\circ$  (as schematically shown in Fig. 1), was used to calculate dislocation density.

### 3. Results

#### 3.1. Initial microstructure

Fig. 2 shows the SEM micrographs taken from the longitudinal section (RD-ND plane) in the ARB processed Ti/Nb composites. Well-defined lamellar structures with flat heterophase interfaces are found when the ARB cycle is below four (Fig. 2a-d). With further ARB processing, due to the different flow stress and work-hardening behavior between the metals, the relatively hard Nb layers begin to neck and even rupture, as indicated by the arrows in Fig. 2e. The preferential necking of the hard constituents and thus the curvature of heterophase interfaces have been commonly found in other multilayered systems [21–23,30,52–57]. The SBs that form an angle of  $\sim 35^\circ$  to RD also become more evident with the increase of ARB cycles (indicated by dashed lines in Fig. 2e-h), due to the accumulated shear stress at the interfaces.

Fig. 3 shows TEM micrographs of the longitudinal section in the composite processed by eight ARB cycles. Some individual layers become discontinuous, leading to the significantly curved interfaces. The distribution of layer thicknesses is quite uneven within both constituents, i.e. the thickness of Ti varies from 100 to 580 nm and that of Nb varies from 130 to 1100 nm. Even in one single layer, the thickness may vary sharply along RD, as indicated by the yellow dashed boundaries of a Ti layer in Fig. 3a. In Ti, the ultrafine grains that are slightly elongated along the heterophase interfaces are observed and the average diameter of the grains is  $\sim 167$  nm. In the Nb layers, narrow deformation bands composed of severely elongated grains are the dominant feature, showing an average lamellar thickness of individual grains of  $\sim 44$  nm. It is noted that in this composite with a nominal layer thickness of 245 nm (Table 1), grain boundaries can be clearly identified in both con-

stituents. The thinner layers consist of even one single grain in the direction perpendicular to the interfaces, whereas the thicker layers consist of 10–20 grains in the same direction. Considering the low recrystallization temperature of pure Ti ( $\sim 550^\circ\text{C}$ ), the specific grain morphology in the current Ti layers partly results from the effect of intermediate annealing. However, recrystallization is more difficult to occur in the refractory metal Nb under the same processing. On the other hand, dynamic recovery and recrystallization may occur in Ti, due to the adiabatic heating (the estimated temperature rise of  $\sim 183^\circ\text{C}$ ) caused by the high rolling speed during ARB and the low thermal conductivity of the metal [45,58] together with the applied roll-bonding temperature of  $300^\circ\text{C}$ . Accordingly, Ti layers exhibit the weaker dislocation contrast compared with Nb. The activation of  $\langle a \rangle$  dislocations accompanied with sparse  $\langle c+a \rangle$  dislocations can be identified in Ti under the double beam condition, as shown in Fig. 3b. Fig. 3c shows an equiaxed subgrain surrounded by the yellow dashed line, suggesting the occurrence of dynamic recovery. Detailed microstructures in the Nb layers (Fig. 3d) reveal that dense dislocations are generated in the deformation bands. Fig. 3e shows the EDS analysis across a heterophase interface between the constituent metals, indicating that the heterophase interface is sharp and no intermetallic compounds are formed. The selected area diffraction patterns in Fig. 3f reveal that the adjacent Ti and Nb grains follow the  $\{10\bar{1}1\}_{\text{Ti}}//\{110\}_{\text{Nb}}$  and  $\langle 11\bar{2}0 \rangle_{\text{Ti}}//\langle 001 \rangle_{\text{Nb}}$  orientation relationship. The high resolution TEM image shows that the interface is coherent and without amorphization (Fig. 3g). Through the geometric phase analysis (GPA) [59], Fig. 3h confirms that the dislocation density in Nb layers is higher than that in Ti.

#### 3.2. Crystallographic texture

ODF sections derived from neutron diffraction of the Ti/Nb composites processed by different ARB cycles are presented in Fig. S2 (Supplementary material). In the starting Ti, a texture component located at a position of  $\varphi_1=90^\circ$ ,  $\Phi=32^\circ$ ,  $\varphi_2=30^\circ$  (Bunge notation) exists, which is close to the  $\{10\bar{1}3\}\langle 30\bar{3}2 \rangle$  orientation. In the ARB processed composites, the dominant texture components in Ti is the  $\{11\bar{2}5\}\langle 10\bar{1}0 \rangle$  orientation located at the position of  $\varphi_1=0^\circ$ ,  $\Phi=32^\circ$ ,  $\varphi_2=0^\circ$ . This is a typical rolling texture, also known as bimodal texture, in hcp structured metals with the  $c/a$  ratio less than 1.633 [58,60]. After the eighth ARB cycle, the  $\{10\bar{1}3\}\langle 11\bar{2}0 \rangle$  orientation located at the position of  $\varphi_1=0^\circ$ ,  $\Phi=32^\circ$ ,  $\varphi_2=30^\circ$  becomes predominant in addition to  $\{11\bar{2}5\}\langle 10\bar{1}0 \rangle$ . These textures agree well with the rolling textures found in Zr of the ARB processed Zr/Nb composites [61]. The starting Nb exhibits the  $\gamma$ -fiber ( $\langle 111 \rangle//\text{ND}$ ) and the R-cubic orientation ( $\langle 001 \rangle\langle 110 \rangle$ ). After the first ARB cycle, textures typically found in cold-rolled bcc materials, namely the  $\alpha$ -fiber ( $\langle 110 \rangle//\text{RD}$ ),  $\gamma$ -fiber as well as R-cubic texture component exist in the Nb layers. With the increasing ARB cycle, the both fibers are weakened, while the R-cubic orientation becomes dominant. The texture components of Nb are similar to that in the ARB processed Cu/Nb [62] and Zr/Nb [61] multilayers.

#### 3.3. Mechanical properties

The stress-strain curves of the Ti/Nb composites, as well as the starting materials, are shown in Fig. 4a. The composites are much stronger but less ductile than the pure metals, which is the typical feature of ultrafine grained materials processed by ARB [63,64]. The Ti/Nb composite fabricated by eight ARB cycles exhibits the highest ultimate tensile strength (UTS) of  $\sim 840$  MPa, while the total elongation (TE) is  $\sim 9.0\%$ . Fig. 4b shows the variation of tensile properties of the Ti/Nb multilayers as a function of ARB cycle. In addition, mechanical properties of CP-Ti [63,64] and Ti/Al [55] multilayers processed via ARB are also shown for comparison. As can

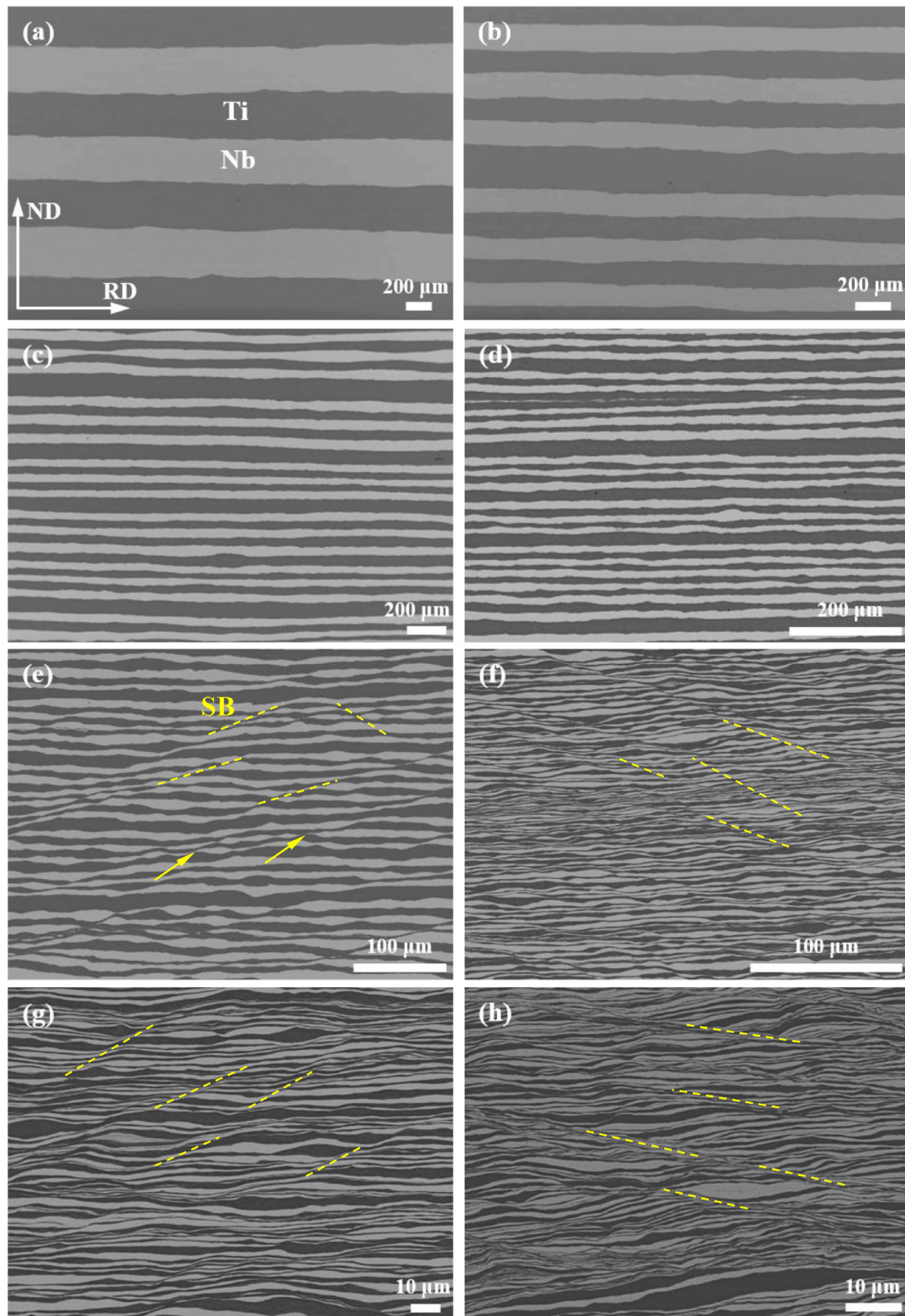


**Fig. 2.** SEM micrographs showing lamellar morphologies in the multilayered Ti/Nb composites produced by different ARB cycles: (a) one, (b) two, (c) three, (d) four, (e) five, (f) six, (g) seven and (h) eight. The Ti layers are shown in dark grey and the Nb layers are in light grey. The arrows indicate necking and fracture of the Nb layers. The dashed lines indicate shear bands.

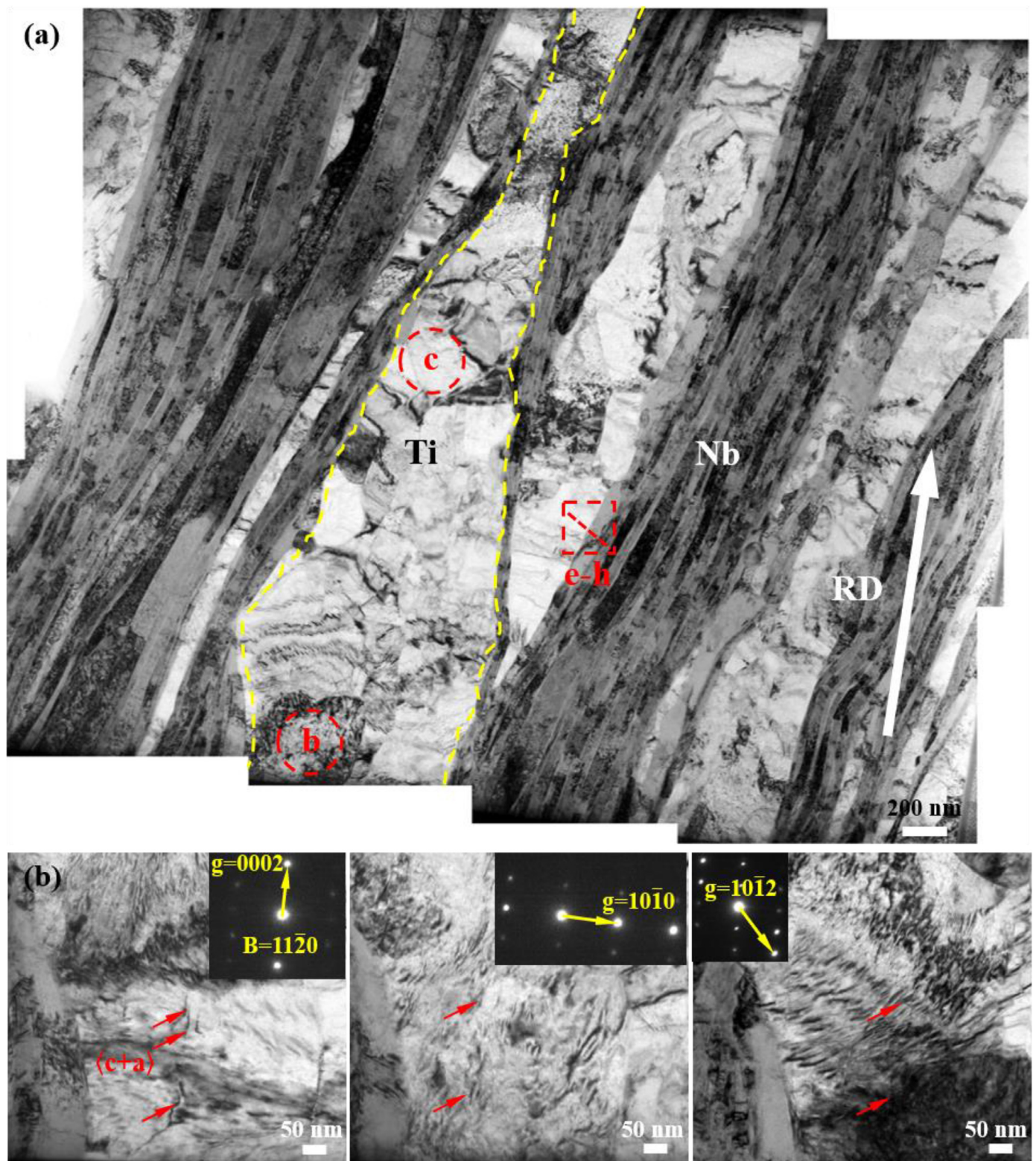


**Fig. 3.** TEM observation of the N8 composite prior to tensile testing: (a) bright-field image, (b) dislocations under different diffraction vector  $g$  in Ti grains with the red arrows indicating the  $\langle c+a \rangle$  dislocations, (c) one subgrain in Ti surrounded by the yellow dashed line and (d) detailed microstructure in Nb. (e) EDS analysis across the heterophase interface (indicated by the red dashed line in (a)). (f) Diffraction patterns of the interface in the same position as (e). (g) HRTEM image of the Ti/Nb interface and the corresponding fast Fourier transform (FFT) patterns and inverse fast Fourier transform (IFFT) fringes. (h) Strain map at the interface area processed from (g).

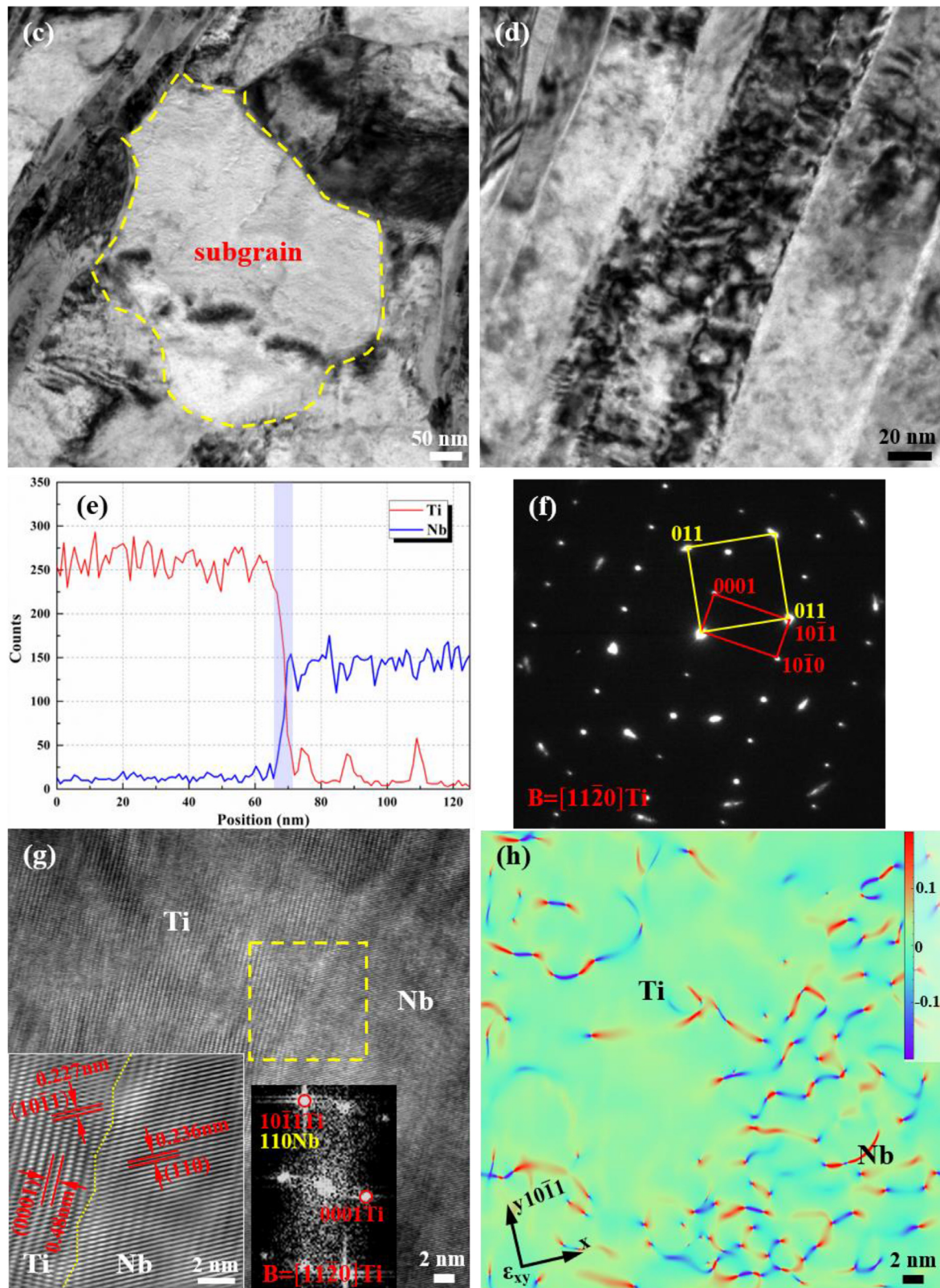
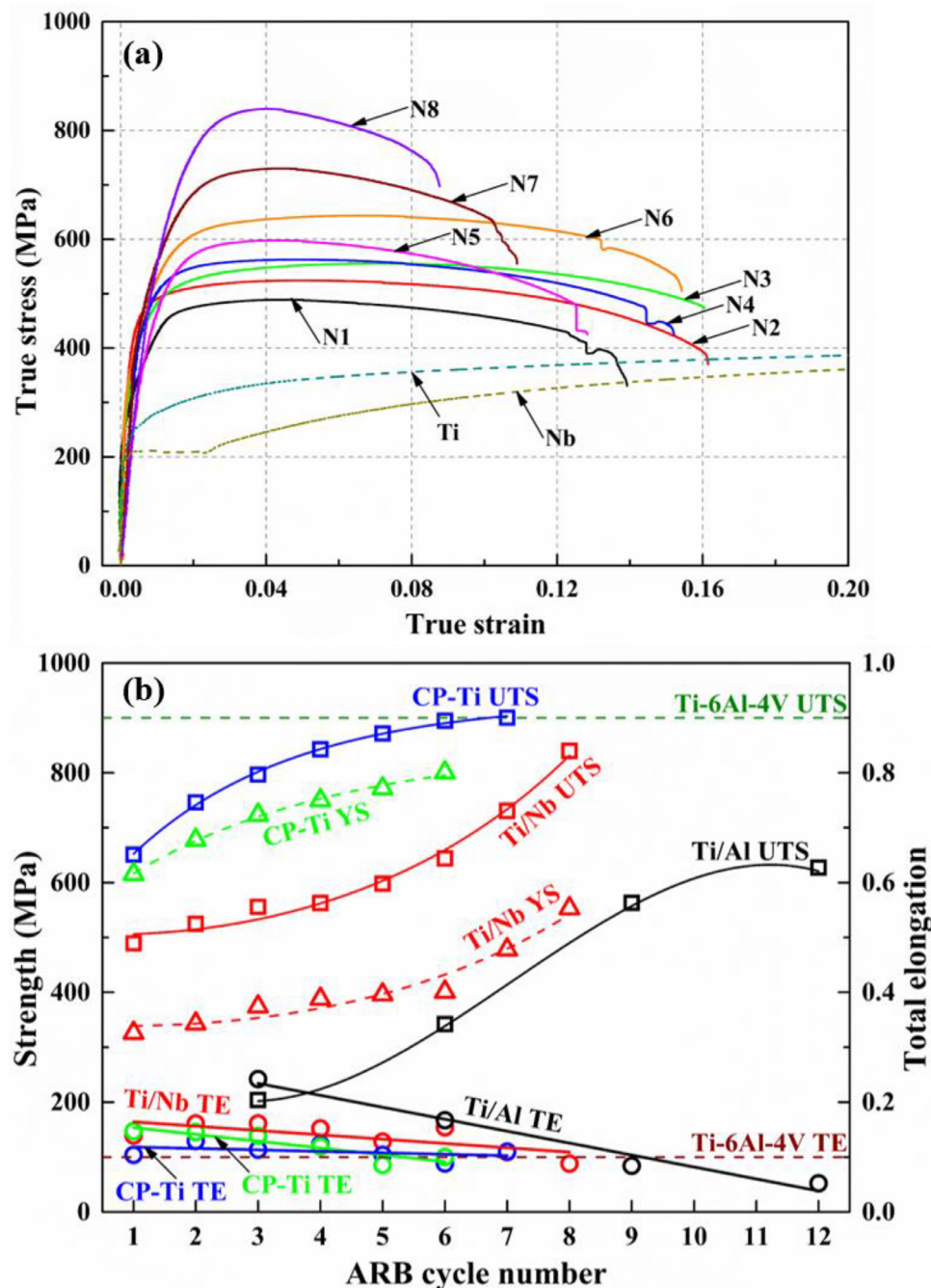


Fig. 3. Continued

be seen, yield strength (YS) and UTS of the studied Ti/Nb increase significantly with the roll bonding processing, namely the increasing rates of the both become larger as a function of the ARB cycle number. For both CP-Ti and Ti/Al multilayers, a sharp increase in strength is found at low cycle numbers and with further roll

bonding the increase rate becomes milder. This tendency is quite common for metallic materials fabricated by the SPD methods, i.e. a gradual saturation of the strengthening effect with accumulated strain [5]. It has been well accepted that strain hardening provides a major role in the strengthening at initial ARB cycles. At higher



**Fig. 4.** Tensile properties of the ARB processed Ti/Nb multilayers: (a) Engineering stress-strain curves, (b) the variation of yield strength, ultimate tensile strength and total elongation with increasing ARB cycles. The data of CP-Ti, Ti/Al multilayers as well as Ti-6Al-4V alloy sheet are also shown for comparison. All materials are under uniaxial tensile testing along RD. YS: 0.2% offset yield strength, UTS: ultimate tensile strength, TE: total elongation.

cycles the contribution from strain hardening becomes less significant and grain refinement plays an important role [64]. Here, it is worth noting that strength in the Ti/Nb composites increases rapidly with increasing ARB cycles. This unsaturated strengthening may be attributed to the fact that the micromechanical behaviors of the constituent metals have been modified with the introduction of heterophase interfaces. On the other hand, the Ti/Nb composites show the lower descending rate of *TE* as the roll bonding number increases, compared with CP-Ti and Ti/Al multilayers. Finally, we note that after the eighth ARB cycle *UTS* and *TE* of the Ti/Nb multilayer are quite close to that of the commercial Ti-6Al-4V alloy sheet [65] (as indicated by dashed lines in Fig. 4b), with the loading direction parallel to RD. That is an indication that the

mechanical properties of our ARB processed composites can be comparable to that of the widely used Ti-6Al-4V.

#### 3.4. Micromechanical behaviors revealed by in-situ HEXRD

Six samples were selected for the *in-situ* HEXRD characterizations. The N1 and N3 samples contain flat constituent layers and the N5-N8 samples are those with significant curvature of heterophase interfaces and SBs. The 1D diffraction profiles of the Ti/Nb multilayers show that all composites are composed of Ti and Nb without the formation of intermetallic compounds (Fig. S3, Supplementary material). By analyzing the integrated intensity of diffraction peaks [66], volume fractions of Ti and Nb, i.e.  $f_{Ti}$  and

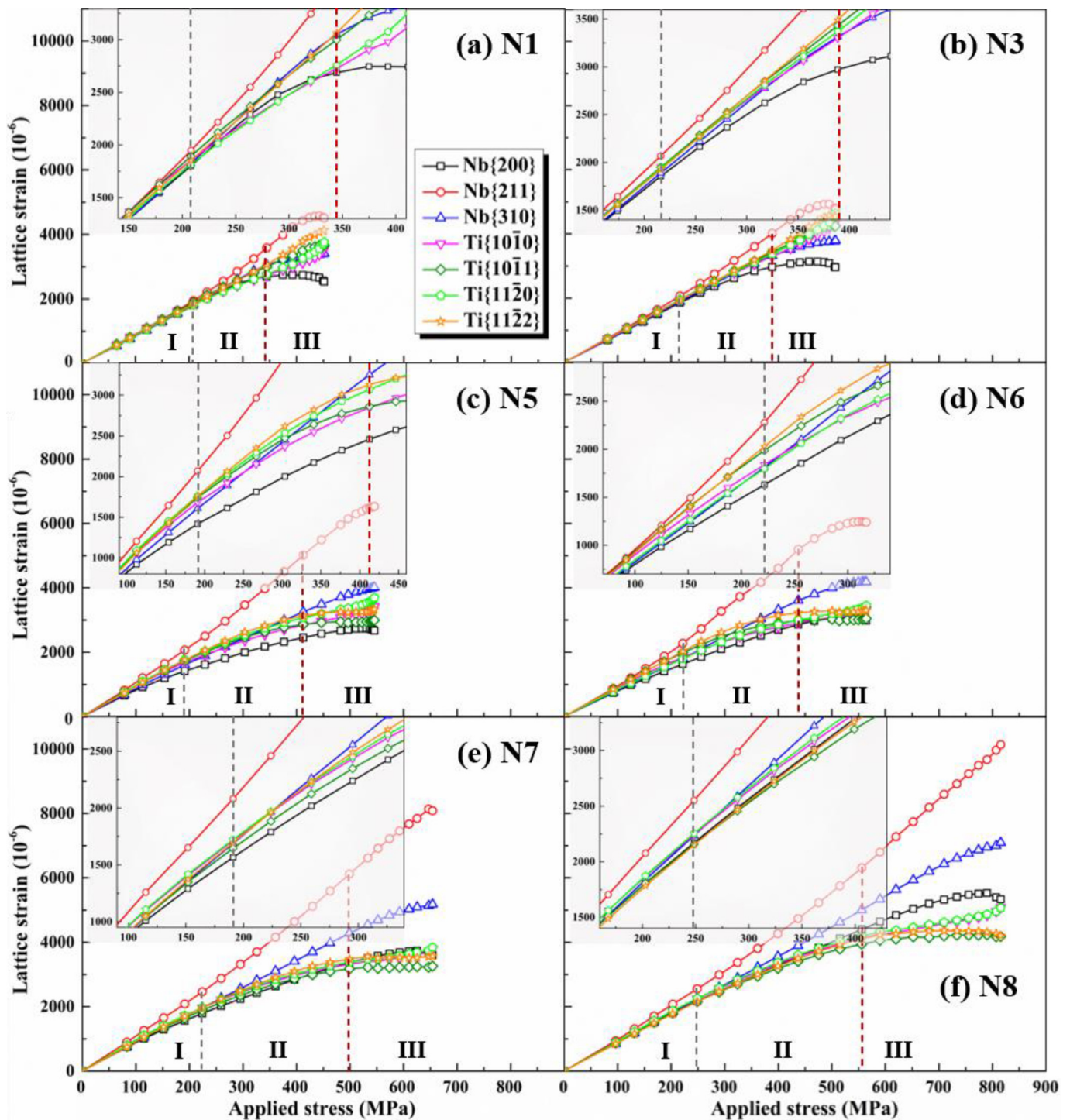


**Fig. 5.** Evolution of lattice strains during uniaxial tensile testing for the Ti/Nb composites processed by (a) one, (b) three, (c) five, (d) six, (e) seven and (f) eight ARB cycles. Uncertainties in the measured lattice strains are below 100 microstrains. The initiations of microscopic and macroscopic plastic deformation are indicated by the grey and wine dashed lines, respectively. I, II and III represent the elastic, elastic-plastic and plastic regimes, respectively. The insets are the enlarged view of the elastic-plastic regime.

$f_{Nb}$  in each composite can be determined (Table S4, Supplementary material), which are consistent with the results obtained from SEM. These values will be used for calculating the total stress of the selected composites.

Fig. 5 shows the lattice strain evolution along the axial direction ( $//LD$ ) for the various  $\{hkl\}$  reflections. In the elastic regime, lattice strains of all  $\{hkl\}$  planes increase linearly with the applied stress in each composite. The elastic constants ( $E$ ) for those planes can be determined by relating lattice strains to the applied stress (Ta-

ble S5, Supplementary material), showing insignificant difference compared with the theoretical values in Table S1 (Supplementary material). This implies negligible intergranular stresses and phase-to-phase interactions in the elastic regime, and, the stress partitioning discussed in the following are mainly originated from the diverse plastic behaviors of the constituent grains/metals. For the N1 multilayer (Fig. 5a), when the applied stress reaches  $\sim 200$  MPa remarkable deviations from linearity of lattice strains are observed for some  $\{hkl\}$  planes. Lattice strains in most  $\{hkl\}$  planes increase

mildly with deformation, except for the Nb {211} plane showing a much higher slope. The slower increase in the Nb {200} lattice strain with deformation indicates that dislocation slip tends to be activated preferentially in the  $\langle 200 \rangle // LD$  grains. Accordingly, load is transferred to the  $\langle 211 \rangle // LD$  Nb grains and Ti grains that exhibit the higher lattice strains. The starting point of microscopic plastic flow within the composite has been indicated by the grey dashed lines in the figure. For the composites processed by more ARB cycles, lattice strain distributions also show the evident strain partitioning among the different  $\{hkl\}$  planes after the microscopic yielding. The discrepancy among the different Nb grains develops with the increase of ARB cycles, which is an indication of the increased grain-to-grain interactions. In the N8 composite, this discrepancy in lattice strains even reaches  $\sim 0.005$  at the maximum applied stress. After six ARB cycles, lattice strains of the Nb {200} grains start to exceed that of Ti grains. As a result, all Nb grains bear the higher lattice strains than the Ti grains. It is worth noting that the discrepancies among the grains and between the constituents show apparent size dependence on the initial layer thickness.

The evolution of dislocation density deduced from the HEXRD measurements for the composites under tensile testing is also analyzed. For all the as-ARBed composites, the dislocation density in Nb is higher than that in Ti (Table S6, Supplementary material), consistent with the TEM observation mentioned above. With increasing deformation, dislocations significantly increase in both constituents. Taking the N8 composite as an example, the initial dislocation densities are  $1.83 \times 10^{14}$  and  $1.01 \times 10^{15} \text{ m}^{-2}$  in Ti and Nb, respectively. At the maximum applied stress (corresponding to 0.042 true strain), Nb shows a dislocation density of  $4.13 \times 10^{15} \text{ m}^{-2}$ , about 8 times that of Ti ( $5.08 \times 10^{14} \text{ m}^{-2}$ ). These observations suggest that Nb layers in the Ti/Nb composites have the much higher capacity of activating dislocations and thus the higher strain hardening than Ti.

### 3.5. Deformation microstructure

TEM observation of the region near the fracture surface of the N8 composite is given in Fig. 6a, showing that the lamellae are less wavy than that prior to tensile testing. However, remarkable deformation has occurred in both constituents, as the average grain size in Ti is reduced from 167 nm to 100 nm while the grain thickness in Nb is reduced from 44 nm to 24 nm. Deformation twins are not identified in the Ti layers, which is attributed to the small size of grains [67]. Through a series of diffraction vector tilting,  $\langle c+a \rangle$  dislocations are always visible (Fig. 6b). This indicates that dislocation glide is the dominant deformation mechanism in Ti. Moreover, the heterophase interface remains coherent after deformation, even though the significant lattice distortion induced by dislocation pile-up occurs at the interface (Fig. 6c).

## 4. Discussion

### 4.1. Stress partitioning among the differently orientated grains and between the constituent metals

To understand micromechanical behavior and thus mechanical properties of the composites, we then choose the N3 and N8 composites as the representatives for discussing stress partitioning in the multilayered structures with different initial layer thicknesses. For Ti layers in the N3 composite (Fig. 7a), once the applied stress reaches 216 MPa, the  $\{10\bar{1}0\}$  grains yield preferentially and then the load begins to transfer to other grains. The intergranular microstress thus increases rapidly with deformation. As more grains yield, the grain-to-grain interaction increases mildly and comes to

a stable level when the applied stress reaches  $\sim 473$  MPa. With further loading, the intergranular stress only slightly fluctuates. For Nb layers (Fig. 7b), the  $\{211\}$  grains bear the highest stress while the  $\{200\}$  grains bear the least load. When the applied stress is below 473 MPa, the evolution of intergranular stress in Nb is similar to that in Ti. Under further loading, grains in Nb are softened and the load is transferred to Ti, leading to a reduction of the grain-to-grain interaction. Such softening of Nb in the N3 composite is ascribed to the necking and fracture of the Nb layers under tensile testing. For Ti layers in the N8 composite (Fig. 7d), the  $\{10\bar{1}0\}$  grains also yield earlier than other grains and the intergranular stress continuously increases with deformation. When the applied stress reaches  $\sim 747$  MPa, the intergranular stress in Ti starts to increase more sharply due to the significant strain hardening of the  $\{11\bar{2}0\}$  grains. For Nb grains in this composite (Fig. 7e), the  $\{211\}$  orientation bears more load than others. When a yield stress of 476 MPa is reached, the intergranular stress in Nb increases dramatically and becomes saturated at around 747 MPa. Moreover, it is worth noting that compared with the N3 specimen, at the elastic stage stress partitioning among the differently oriented grains in the individual metals is more pronounced in the N8 specimen.

The average stresses along the LD in Ti and Nb, i.e.  $\bar{\sigma}_{\text{Nb}}$  and  $\bar{\sigma}_{\text{Ti}}$ , are calculated by the weighted average of the axial stress in different  $\{hkl\}$  grains of the respective phases [68], as described in Note (i) of the Supplementary material. The total stress ( $\sigma_{\text{T}}$ ) of the Ti/Nb composites is then determined by the mixture law [69], i.e.,  $\sigma_{\text{T}} = f_{\text{Ti}} \bar{\sigma}_{22}^{\text{Ti}} + f_{\text{Nb}} \bar{\sigma}_{22}^{\text{Nb}}$ , where  $\bar{\sigma}_{22}^{\text{Ti}}$  and  $\bar{\sigma}_{22}^{\text{Nb}}$  are the average stresses of Ti and Nb, respectively. Fig. 7c and f show the evolution of average stress of each constituent, total stress and interphase microstress as a function of the applied true strain in the N3 and N8 composites, respectively. The calculated total stress agrees well with the applied stress. In the elastic regime, load partitioning between the constituents already exists in both composites and Nb bears more load than Ti. Ti preferentially yields in the N3 and N8 composites at an applied stress of 318 and 437 MPa, respectively. For the N3 composite, with further loading, Nb is softened quickly and the load is transferred to Ti, leading to the reduced phase-to-phase interaction. When the applied stress reaches  $\sim 495$  MPa, Ti becomes stiffer than Nb and the phase-to-phase interaction increases again. For the N8 composite, Nb always acts as the stiffer constituent, leading to the increased interphase stress. At an applied load of 790 MPa, stress partitioning between the constituents starts to decrease due to the saturated strain hardening of Nb.

### 4.2. Strengthening and toughening mechanisms of the composites

Based on the microstructural evolution of the Ti/Nb multilayers during tensile loading, the origin of strength in the composites can be summarized as follows: solid-solution strengthening ( $\sigma_{\text{s}}$ ), grain-boundary strengthening ( $\sigma_{\text{g}}$ ), dislocation strengthening ( $\sigma_{\text{d}}$ ) and heterophase interface strengthening ( $\sigma_{\text{i}}$ ). Thus, the flow stress ( $\sigma$ ) of the individual constituents is calculated as:

$$\sigma = \sigma_0 + \sigma_{\text{s}} + \sigma_{\text{g}} + \sigma_{\text{d}} + \sigma_{\text{i}} \quad (3)$$

where  $\sigma_0$  is the friction stress. A column chart is shown to visualize the individual contributions to the UTS of each constituent metal, as shown in Fig. 8a and b, respectively. The detailed calculation of strength contributions is given in Note (ii) of the Supplementary material. The UTS value is derived from the *in-situ* HEXRD analysis, i.e. the average stresses of each constituent. Evidently, as the ARB cycle number increases the rapid strengthening of the composites is mainly ascribed to the strengthening of Nb that originates from dislocations, grain boundaries and heterophase interfaces. For the Ti layers, the dominant strengthening originates from grain boundaries, accounting for  $\sim 60\%$  of the UTS. This is due to the limited capability of dislocation multiplications in Ti, as confirmed

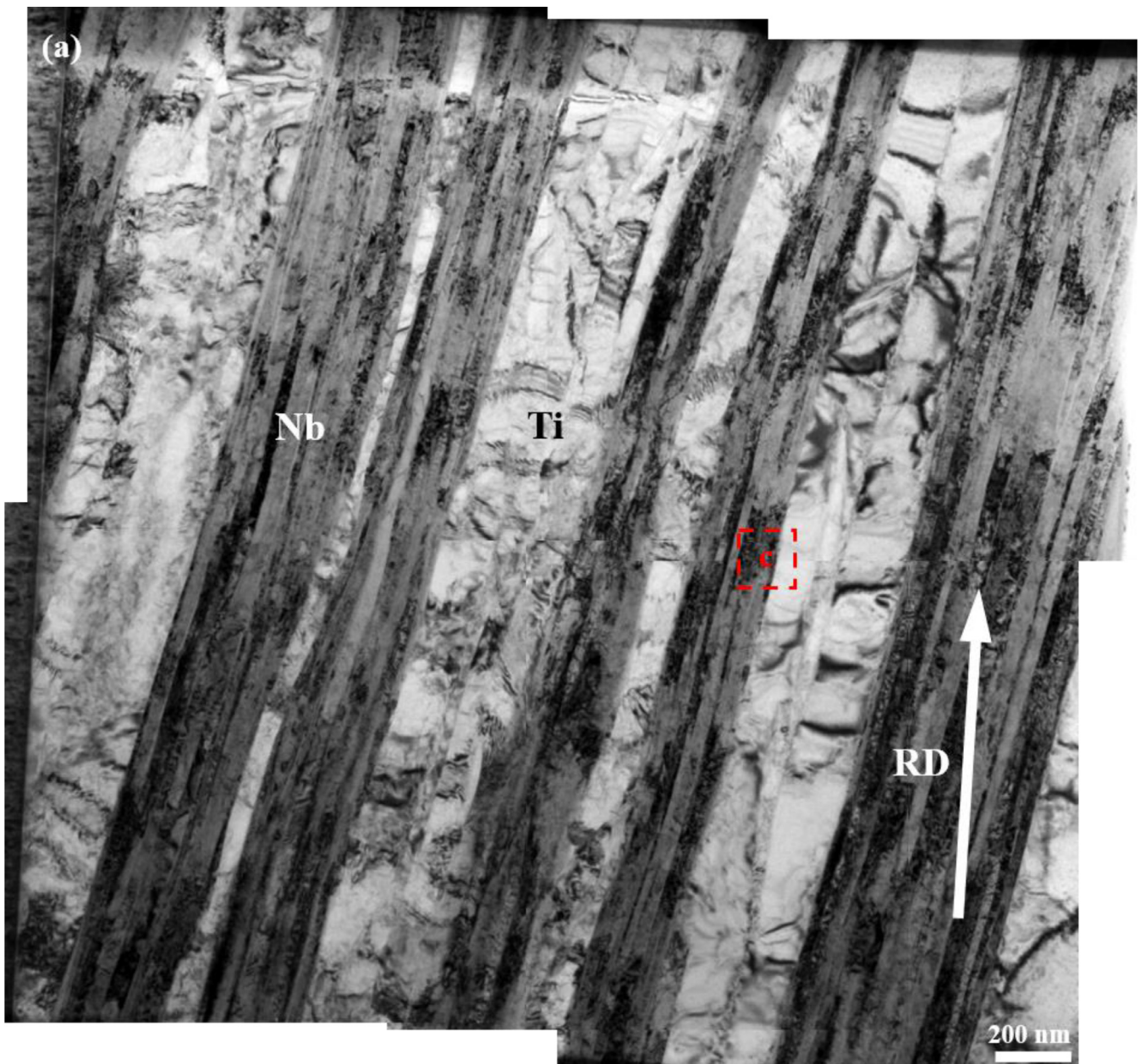


**Fig. 6.** TEM observation of the region close to fracture surface of the N8 composite after tensile testing: (a) bright-field image, (b) dislocations under different diffraction vector  $g$  in Ti, with the red arrows indicating the  $(c + a)$  dislocations, (c) IFFT fringes of the Ti/Nb interface obtained from the selected area in (a).

by the analysis of dislocation density obtained from both HEXRD and TEM characterizations. For the Nb layers,  $\sigma_d$  and  $\sigma_i$  are the dominant strength contributions, accounting for ~80% of the *UTS*. Intrinsically,  $\sigma_i$  originates from the inhibition of dislocation slip by the heterophase interfaces, leading to dislocation pile-up at the interfaces. Thus, it is reasonable that as a function of ARB cycle number, the variation tendencies of contributions from the two mechanisms, i.e. dislocation strengthening and interface strengthening, are correlated with each other in the composites. In addition, with increasing ARB cycles the increment of grain boundary strengthening in Ti is less significant than that in Nb. This is because the grain size in Ti have been remarkably reduced during the first ARB cycle, i.e. from 48.8  $\mu\text{m}$  to 301 nm, and then mildly decreased to 167 nm after eight ARB cycles. In the Nb layers, however, the grain thickness along the ND of the composites is significantly decreased from 13.8  $\mu\text{m}$  prior to roll bonding to 2.5  $\mu\text{m}$  after one ARB cy-

cle, and then to 44 nm after eight cycles (Fig. S4 and Table S7, Supplementary material). One may also note that the *UTS* of Ti in the N6 composite is lower than that in the N3 and N8 composites. Actually, the average stress of the Ti layers in the N6 sample stands between that of the N5 and N8 samples (Fig. S5, Supplementary material), suggesting that the data from the composite processed by six ARB cycles is credible. The softer Ti in this composite is ascribed to the stress/strain accommodation between the constituent metals during co-deformation, which will be discussed in Section 4.3.

Strain hardening behavior of the individual constituents derived from lattice strain evolutions of the composites is also examined. For a multilayered structure, the apparent strain hardening can be expressed as [70]:

$$\frac{\partial \sigma}{\partial \varepsilon_{\text{tot}}} = f_{\text{Ti}} E^{\text{Ti.hkl}} \left( \frac{\partial \varepsilon_{\text{elastic}}^{\text{Ti.hkl}}}{\partial \varepsilon_{\text{tot}}} \right) + f_{\text{Nb}} E^{\text{Nb.hkl}} \left( \frac{\partial \varepsilon_{\text{elastic}}^{\text{Nb.hkl}}}{\partial \varepsilon_{\text{tot}}} \right) \quad (4)$$

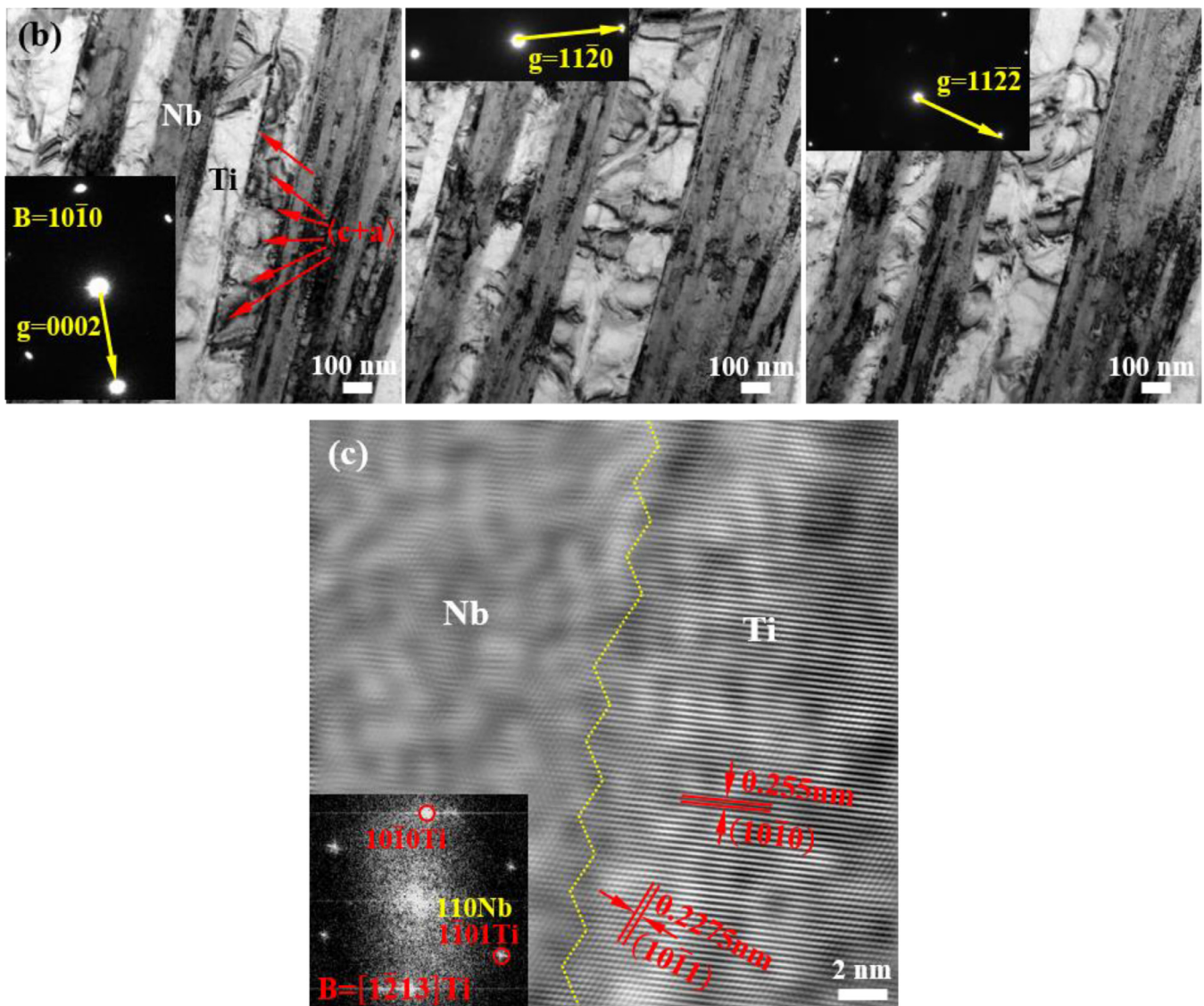


Fig. 6. Continued

where  $\sigma$  is the global stress,  $\varepsilon_{\text{tot}}$  is the total strain applied on the composite,  $(E^{\text{Ti,hkl}}, E^{\text{Nb,hkl}})$  and  $(\varepsilon_{\text{elastic}}^{\text{Ti,hkl}}, \varepsilon_{\text{elastic}}^{\text{Nb,hkl}})$  are the elastic modulus and elastic lattice strain of Ti and Nb along the  $\langle hkl \rangle$  direction, respectively. Fig. 9a shows the global strain hardening  $(\partial\sigma/\partial\varepsilon_{\text{tot}})$  obtained from the true stress-strain curves during *in-situ* tensile tests, in which similar strain hardening responses appear in the composites with different ARB cycles. After the elastic regime, the  $(\partial\sigma/\partial\varepsilon_{\text{tot}})$  decreases rapidly with increasing load. The critical stress for the elastic-plastic transition is indicated by arrow for each composite. The applied stress at the macroscopic yielding point for the N1, N3, N6 and N8 composites are 264, 317, 330 and 439 MPa, respectively. To further illuminate the contribution of individual metals to the global strain hardening, the evolution of  $(\partial\varepsilon_{\text{elastic}}/\partial\varepsilon_{\text{tot}})$  along LD for some different lattice planes are presented in Fig. 9b-f, respectively. In particular, the Nb  $\{211\}$  plane shows an increasing  $(\partial\varepsilon_{\text{elastic}}/\partial\varepsilon_{\text{tot}})$  at the initial stage of deformation, suggesting that the load transfer to Nb  $\{211\}$  grains even occurs in the elastic regime due to the complex elastic interactions among grains and the strong constraint of heterophase interfaces. During the subsequent deformation, the  $\{211\}$  orientation shows the higher  $(\partial\varepsilon_{\text{elastic}}/\partial\varepsilon_{\text{tot}})$  compared with other grains. Moreover, the stress at which the  $\{211\}$  grains start to yield is quite

close to that of the corresponding composites, indicating that the  $\{211\}$  grains play an important role in the strengthening of the bulk material. Interestingly, in the N6 and N8 composites all the lattice planes of Ti as well as the  $\{200\}$  plane of Nb show a slow decline of the  $(\partial\varepsilon_{\text{elastic}}/\partial\varepsilon_{\text{tot}})$  during plastic deformation. This may be attributed to the massive activation of the  $\langle c+a \rangle$  dislocations in Ti, as evidenced by the TEM observation in the N8 composite (Fig. 6). For the Nb  $\{200\}$  grains that yield preferentially than the  $\{211\}$  grains, the strong interactions among dislocations are responsible for the steady evolution of the  $(\partial\varepsilon_{\text{elastic}}/\partial\varepsilon_{\text{tot}})$  with external loading. These behaviors can extend strain hardening of the bulk composites to a wider deformation range and thus postpone the onset of necking.

#### 4.3. Effect of shear banding on the co-deformation of constituent metals

Stress partitioning within the multilayered structure is important for releasing strain localization and overcoming deformation incompatibility between the constituents. For the Ti/Nb multilayers in which the heterophase interfaces remain flat, during uniaxial tensile testing the Nb layers act as the stronger constituent and

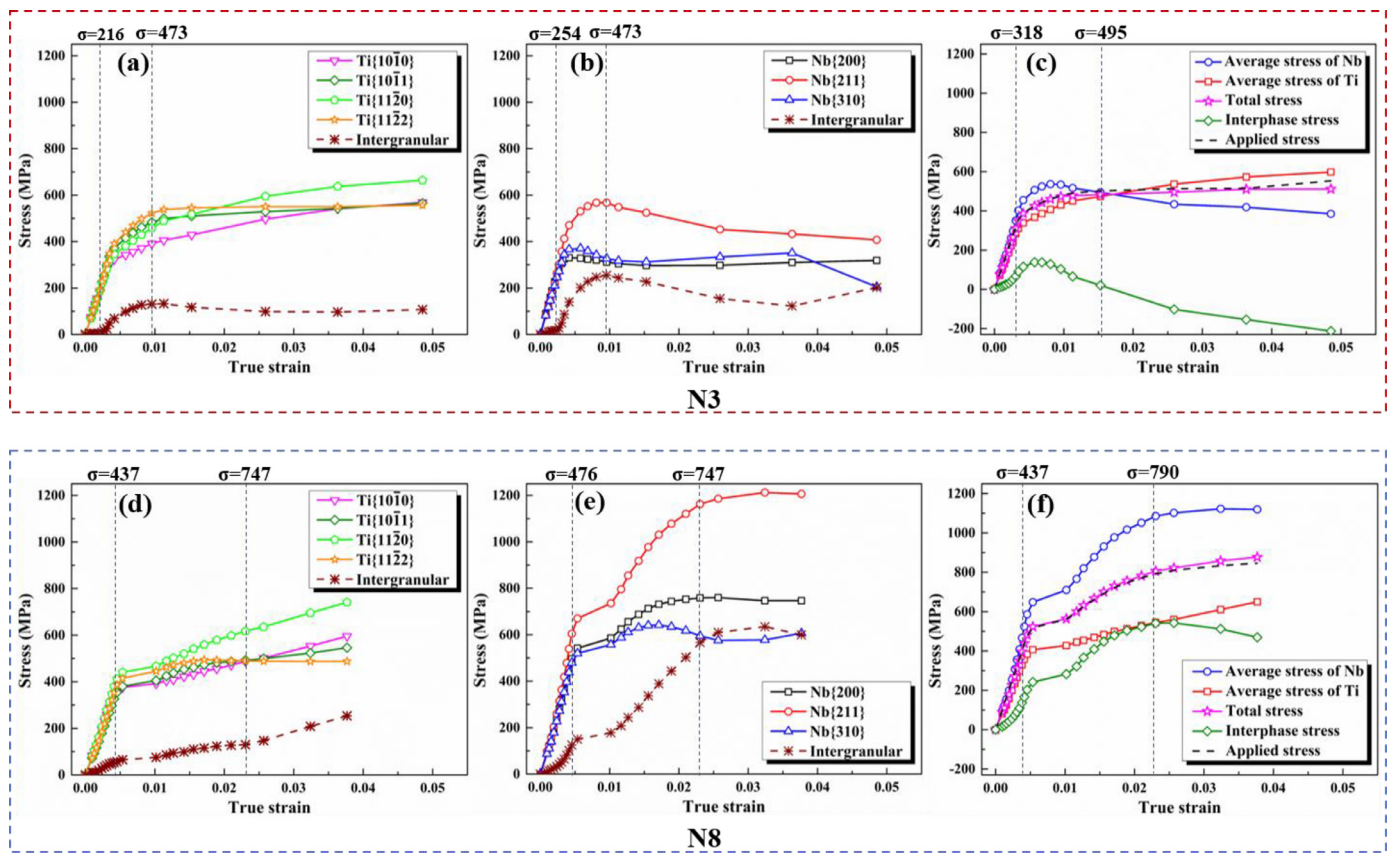


Fig. 7. Stress along LD ( $\sigma_{22}$ ) of the selected  $\{hkl\}$  planes and intergranular microstress as a function of applied true strain in (a) Ti and (b) Nb of the N3 composite. Stress partitioning among the differently orientated grains in Ti and Nb of the N8 composite is shown in (d) and (e), respectively. The average stress of each constituent, total stress and interphase microstress as a function of true strain in the N3 and N8 composites are shown in (c) and (f), respectively. The  $\sigma$  values presented on the top of each plot are the applied stress and their unit is MPa. Intergranular stress in individual metals is calculated as the maximum difference in stress among the different grains. Interphase stress is calculated as the difference in stress between the constituents.

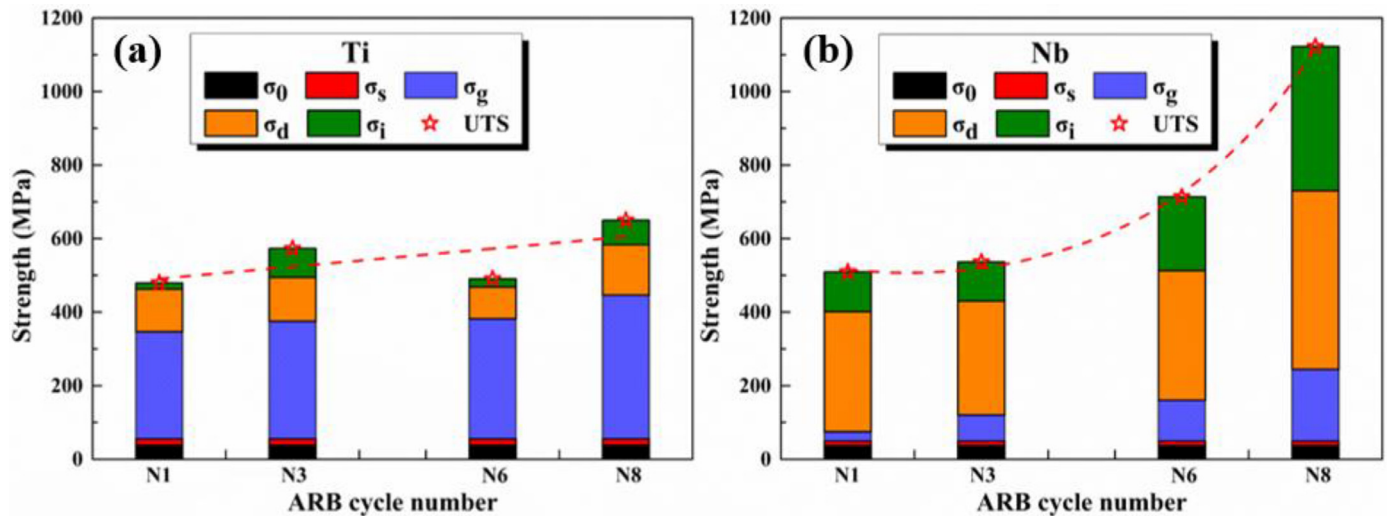
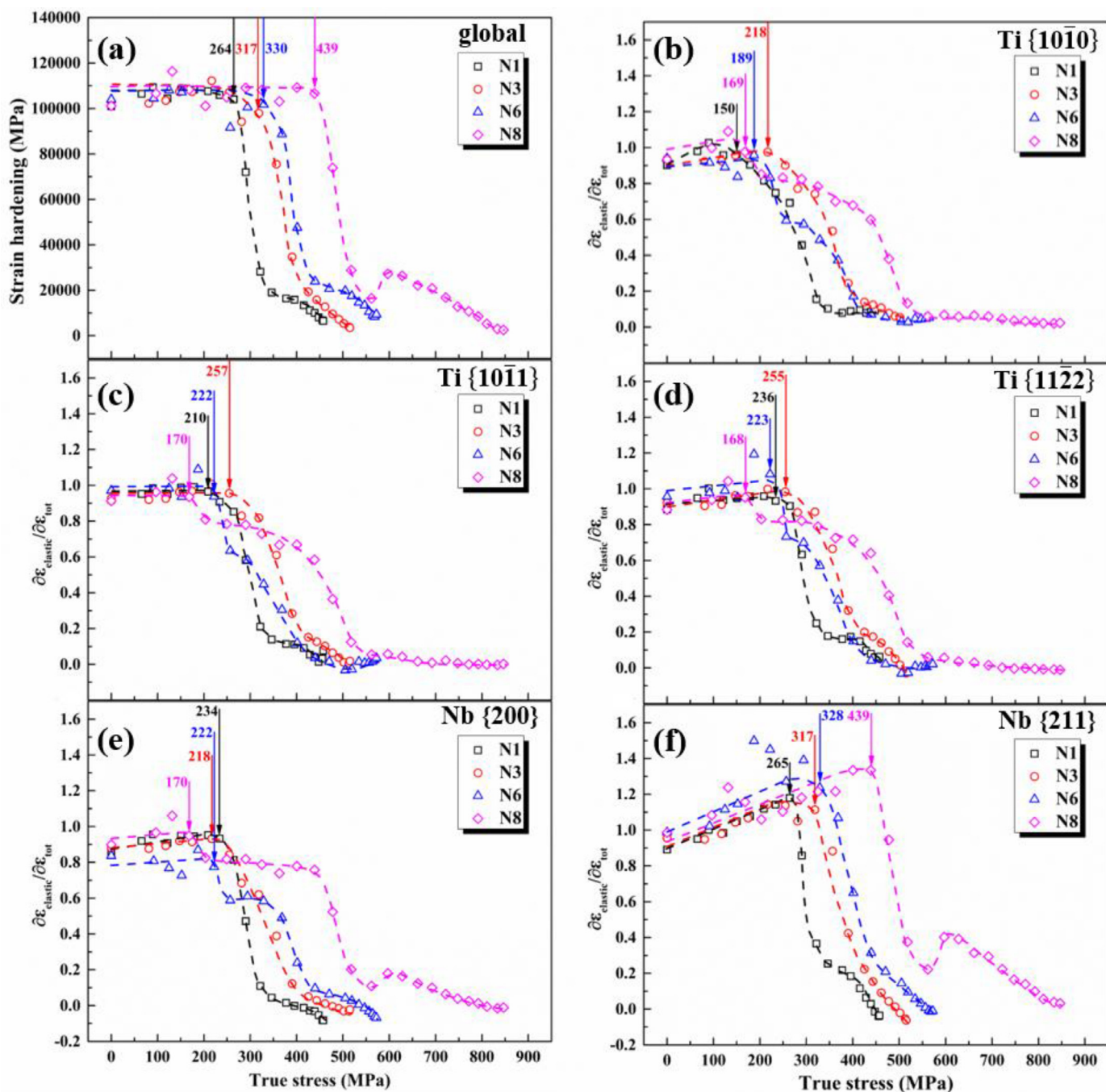


Fig. 8. Strength contributions of each constituent metal to their respective ultimate tensile strength in N1, N3, N6 and N8 composites: (a) Ti and (b) Nb.  $\sigma_0$ : friction stress,  $\sigma_s$ : solid-solution strengthening,  $\sigma_g$ : grain-boundary strengthening,  $\sigma_d$ : dislocation strengthening,  $\sigma_i$ : heterophase interface induced strengthening, UTS: ultimate tensile strength.

sustain more stress. With further deformation, Nb becomes softened due to necking and fracture, while Ti acts as the stronger constituent to carry more load, as shown in Fig. 7a-c. For the composites processed after more ARB cycles (with significantly curved interfaces), due to the hardening of Nb as well as the promoted interactions between the constituent metals resultant from the ac-

tivation of shear bands, Nb always acts as the stronger constituent under deformation (Fig. 7d-f). Considering that the Ti  $\langle 10\bar{1}0 \rangle // LD$  and Nb  $\langle 211 \rangle // LD$  grains show the maximum relative integral intensities among the studied lattice reflections in individual metals (Fig. S6, Supplementary material), their stress tensors expressed in the  $S_1$ - $S_2$ - $S_3$  sample coordinates for the N3 composite are dis-



**Fig. 9.** (a) Evolution of global strain hardening ( $\partial\sigma/\partial\epsilon_{tot}$ ) of the N1, N3, N6 and N8 composites with true stress. Evolution of increasing rate in lattice strain ( $\partial\epsilon_{elastic}/\partial\epsilon_{tot}$ ) for the differently oriented grains is also shown: (b) Ti  $\{10\bar{1}0\}$ , (c) Ti  $\{10\bar{1}1\}$ , (d) Ti  $\{11\bar{2}2\}$ , (e) Nb  $\{200\}$  and (f) Nb  $\{211\}$ .

played in Table 2. For the elastically deformed composite, as the Poisson's ratio of Nb ( $-0.37$ ) is larger than that of Ti ( $-0.32$ ), the former will shrink more in the plane perpendicular to LD. Accordingly, under the constraint of heterophase interfaces a positive stress component along ND ( $\sigma_{33}$ ) and a negative component along TD ( $\sigma_{11}$ ) appear in Nb and Ti, respectively. This leads to a conversion of the applied uniaxial stress into biaxial stresses in both metals. In the elastic-plastic regime, this stress state is maintained for accommodating deformation between the constituents, which agrees with the results in multilayered Ti/Al composites [6]. When plastic regime is reached, the triaxial stresses, i.e. the significant stress components on the main diagonal of the stress tensor, are present in both constituents. For the N8 composite (Table 3), the

biaxial stresses have also been identified in both Ti and Nb in the elastic regime, and the stress state is converted to triaxial in the elastic-plastic regime, which is different from that in the N3 composite and the Ti/Al multilayers [6]. As the N8 specimen is featured with abundant shear bands, the stress tensors expressed in the  $R_1$ - $R_2$ - $R_3$  shear banding coordinates (Fig. 10a) of this composite is also examined. As presented in Table S8 of the Supplementary material, at various applied stresses the  $\sigma_{33}$  in the shear banding coordinates is remarkably higher than that in the sample coordinates. This strong interaction between the neighboring metals in the shear banded zone thus leads to the complex stress states of each constituent.

**Table 2**

The stress tensors expressed in the  $S_1$ - $S_2$ - $S_3$  sample coordinates of the Ti  $\langle 10\bar{1}0 \rangle // LD$  and Nb  $\langle 211 \rangle // LD$  grains in the N3 composite under uniaxial tensile testing. The main diagonal components  $\sigma_{11}$ ,  $\sigma_{22}$  and  $\sigma_{33}$  represent stresses along the TD, RD and ND, respectively. For clarity, only the stress tensors at one selected applied stress for each deformation regime are given. The dominant stress components on the main diagonal are shown in bold.

Regime	Applied stress (MPa)	Stress tensor of Ti $\{10\bar{1}0\}$ (MPa)	Stress tensor of Nb $\{211\}$ (MPa)
Elastic	281	$\begin{pmatrix} -51.8 & 8.0 & -4.6 \\ 8.0 & \mathbf{242.4} & 17.0 \\ -4.6 & 17.0 & -14.1 \end{pmatrix}$	$\begin{pmatrix} 17.9 & 11.5 & -8.7 \\ 11.5 & \mathbf{300.4} & 24.7 \\ -8.7 & 24.7 & \mathbf{47.6} \end{pmatrix}$
Elastic-plastic	355	$\begin{pmatrix} -67.8 & 9.3 & -5.7 \\ 9.3 & \mathbf{299.2} & 9.2 \\ -5.7 & 9.2 & -32.6 \end{pmatrix}$	$\begin{pmatrix} 36.3 & 17.0 & -15.9 \\ 17.0 & \mathbf{412.5} & 24.1 \\ -15.9 & 24.1 & \mathbf{73.6} \end{pmatrix}$
Plastic	440	$\begin{pmatrix} -82.8 & 10.1 & 0.0 \\ 10.1 & \mathbf{355.5} & -3.4 \\ 0.0 & -3.4 & -56.1 \end{pmatrix}$	$\begin{pmatrix} \mathbf{66.3} & 23.0 & -31.5 \\ 23.0 & \mathbf{552.1} & 25.1 \\ -31.5 & 25.1 & \mathbf{130.1} \end{pmatrix}$

**Table 3**

The stress tensors expressed in the  $S_1$ - $S_2$ - $S_3$  sample coordinates of the Ti  $\langle 10\bar{1}0 \rangle // LD$  and Nb  $\langle 211 \rangle // LD$  grains in the N8 composite under uniaxial tensile testing. The main diagonal components  $\sigma_{11}$ ,  $\sigma_{22}$  and  $\sigma_{33}$  represent stresses along the TD, RD and ND, respectively. For clarity, only the stress tensors at one selected applied stress for each deformation regime are given. The dominant stress components on the main diagonal are shown in bold.

Regime	Applied stress (MPa)	Stress tensor of Ti $\{10\bar{1}0\}$ (MPa)	Stress tensor of Nb $\{211\}$ (MPa)
Elastic	324	$\begin{pmatrix} -68.1 & -11.9 & -6.0 \\ -11.9 & \mathbf{258.1} & 30.9 \\ -6.0 & 30.9 & -22.1 \end{pmatrix}$	$\begin{pmatrix} 29.4 & -4.7 & -4.9 \\ -4.7 & \mathbf{362.8} & 45.3 \\ -4.9 & 45.3 & \mathbf{79.4} \end{pmatrix}$
Elastic-plastic	437	$\begin{pmatrix} -78.8 & -7.5 & -9.4 \\ -7.5 & \mathbf{340.7} & 20.4 \\ -9.4 & 20.4 & -42.5 \end{pmatrix}$	$\begin{pmatrix} \mathbf{54.8} & 7.7 & -11.8 \\ 7.7 & \mathbf{539.0} & 48.3 \\ -11.8 & 48.3 & \mathbf{110.6} \end{pmatrix}$
Plastic	733	$\begin{pmatrix} -47.7 & -5.4 & 13.2 \\ -5.4 & \mathbf{455.7} & -0.8 \\ 13.2 & -0.8 & -91.0 \end{pmatrix}$	$\begin{pmatrix} \mathbf{150.6} & 52.1 & -46.3 \\ 52.1 & \mathbf{1077.9} & 48.8 \\ -46.3 & 48.8 & \mathbf{245.7} \end{pmatrix}$

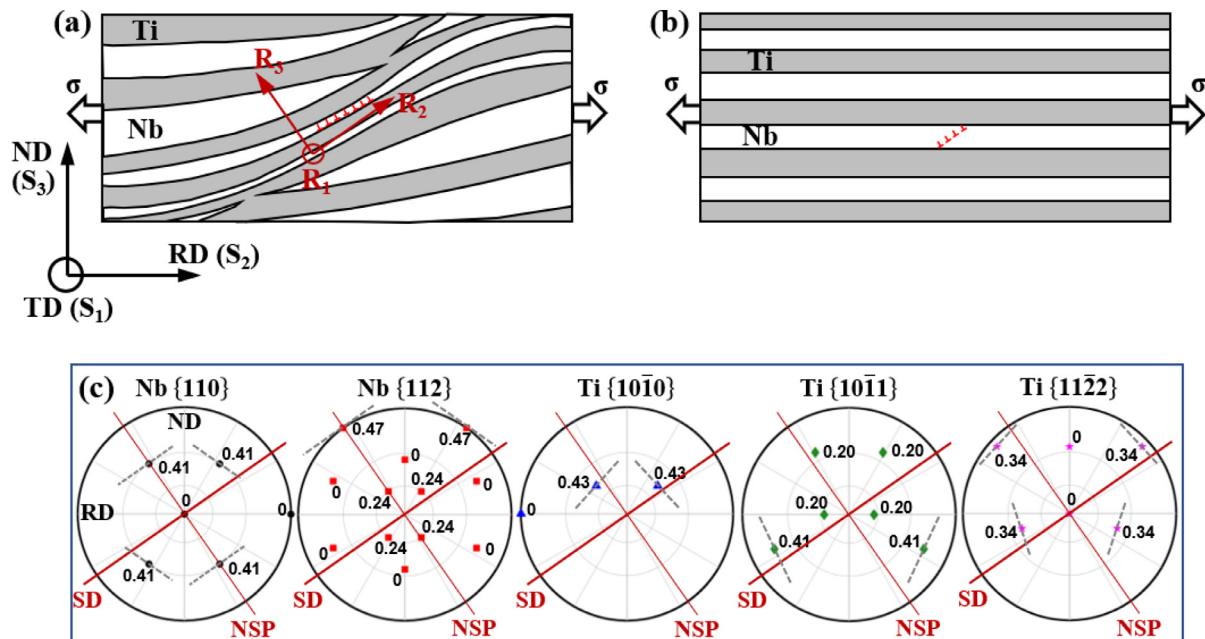


**Fig. 10.** Schematic sketch illustrating the effect of heterophase interfaces on the micromechanical behavior of a multilayered structure under uniaxial tensile loading: (a) the longitudinal section with SBs and (b) the longitudinal section without SBs. (a) also shows the  $R_1$ - $R_2$ - $R_3$  shear banding coordinates constructed by the  $R_2$  (shear direction),  $R_3$  (normal direction of the shear plane) and  $R_1$  axes. (c) Stereographic projection of the slip planes in Ti ( $\varphi_1=0^\circ$ ,  $\Phi=32^\circ$ ,  $\varphi_2=0^\circ$ ) and Nb ( $\varphi_1=0^\circ$ ,  $\Phi=0^\circ$ ,  $\varphi_2=45^\circ$ ) single crystals. Only slip systems with the maximum Schmid factors are presented. The numbers adjacent to the notations are the Schmid factors of individual slip variants, as given in Table S9 and S10 in the Supplementary material. The dashed lines represent the traces of slip planes of dislocations. RD: rolling direction, ND: normal direction of the rolled plane, SD: shear direction, NSP: normal direction of the shear plane.

As mentioned above, for the ARB processed composites the predominant texture components are  $\{11\bar{2}5\}\langle 10\bar{1}0\rangle$  and  $\{001\}\langle 110\rangle$  in Ti and Nb, respectively. The activation of various slip systems under the uniaxial loading along RD is then estimated for the respective metals. As listed in Table S9 of the Supplementary material, the  $\{001\}\langle 110\rangle$  orientation show Schmid factors of 0.41 and 0.47 for the  $\{110\}\langle 111\rangle$  and  $\{112\}\langle 111\rangle$  systems, respectively. Thus, both systems can be activated in the Nb layers. For the  $\{11\bar{2}5\}\langle 10\bar{1}0\rangle$  orientation in Ti, Schmid factors of the prismatic  $\langle a\rangle$  and pyramidal  $\langle c+a\rangle$  systems are 0.43 and 0.41, respectively (Table S10, Supplementary material). This indicates that slip on these systems may occur, as also evidenced by the TEM observation. Furthermore, trace analysis [71] is used to analyze the slip activities within the multilayered structure. As shown in Fig. 10c, some slip variants show the slip plane parallel to the shear direction (SD) of shear bands. That means due to the inclination of metals within the shear banded region, the moving dislocations may have the longer mean free path compared with that in multilayers without shear banding (Fig. 10b). It has been well known that dislocations emitted from a dislocation source inside one grain will propagate until they reach grain boundaries, and, the boundaries hinder further dislocation motion and emission of more dislocations [72]. The Ti/Nb heterophase interfaces here also act as grain boundaries. Therefore, the shear bands that are inclined to RD are favorable for dislocation multiplication and motion in the multilayered structure. This leads to high density of dislocations in the individual constituents and contributes to high strength of the N8 composite while a total elongation of 9.0% is maintained.

## 5. Conclusions

In the present study, multilayered Ti/Nb composites with different initial layer thicknesses were fabricated by ARB. The micromechanical behaviors of the composites under uniaxial tensile tests were investigated by *in-situ* HEXRD measurements in combination with TEM observations, so as to reveal deformation mechanisms of the multilayered structure with and without shear banding. A fundamental understanding of load partitioning and strengthening mechanisms of the multilayered composites as well as co-deformation of the constituents has been accessed. The main conclusions are summarized as follows:

- 1) The multilayered Ti/Nb composites with immiscible heterophase interfaces are produced by ARB. With the increase of roll bonding cycles, shear bands that form an angle of  $\sim 35^\circ$  to RD become more evident in the significantly strengthened composites. The Ti/Nb multilayer fabricated by eight ARB cycles exhibits an ultimate tensile strength of  $\sim 840$  MPa and a total elongation of  $\sim 9\%$ .
- 2) Under uniaxial tensile loading, the Nb layers are subjected to much higher stress than the Ti layers. The rapid strengthening of the composites with increasing ARB cycles is mainly ascribed to the strengthening of Nb that originates from dislocations, grain boundaries and heterophase interfaces. Thereinto, the dislocation strengthening and heterophase interfaces strengthening contribute most to the UTS of Nb. The Nb  $\{211\}$  grains mainly contribute to the global strain hardening of the composites. Besides, for the composites fabricated by more ARB cycles, grains in Ti show a slow decline of the  $(\partial\varepsilon_{\text{elastic}}/\partial\varepsilon_{\text{tot}})$  with deformation, which extends the strain hardening of the multilayers to a wider deformation range and postpones the onset of necking.
- 3) For the N3 composite initially incorporating flat heterophase interfaces, the applied uniaxial stress is converted into the biaxial stresses in elastic regime. When plastic regime is reached, the triaxial stresses are present in both constituents. For the N8

composite initially featured with extensive shear bands, significant load partitioning among the grains and between the constituent metals even appears in elastic regime. The strong interaction between Ti and Nb in the shear banded zone results in an early conversion of the stress state from biaxial in the elastic regime to triaxial in the elastic-plastic and plastic regimes.

- 4) Within the shear banded zone dislocations are prone to slip along the shear direction, promoting dislocation multiplication and motion in the multilayered structure. This is conducive to the strength elevation of the composites processed by multiple ARB cycles, while a satisfactory ductility can still be maintained.

## Disclaimer

Certain trade names and company products are identified in order to specify aspects of the experimental procedure adequately. Such identification is not intended to imply recommendation or endorsement by National Institute of Standards and Technology, nor is it intended to imply that the materials or equipment identified are necessarily the best available for the purpose.

## Declaration of Competing Interest

The authors declare that they have no known competing financial interests or personal relationships that could have appeared to influence the work reported in this paper.

## Acknowledgements

S. Jiang and N. Jia acknowledge the financial support from the National Natural Science Foundation of China (No. 51922026), the Fundamental Research Funds for the Central Universities (Nos. N2002005, N2007011) and the 111 Project (No. B20029). R. Lin Peng and J.J. Moverare acknowledge the financial support from Swedish Government Strategic Research Area in Materials Science on Functional Materials at Linköping University (Faculty Grant SFO-Mat-LiU 2009-00971). The authors are grateful to the beam time at P21.2 beamline of PETRA III, DESY, Germany under experiment No. I-20190164 EC and BT8 diffractometer of NIST, USA. The authors also would like to thank Mr. H.R. Yi at Northeastern University for preparing the multilayered composites, Dr. W.Y. Liu at ZKKF (Beijing) Science & Technology Co., Ltd for TEM characterization and Dr. K. Máthi at Charles University for the application of the CMWP method. S. Jiang thanks the support of China Scholarship Council.

## Supplementary materials

Supplementary material associated with this article can be found, in the online version, at doi:[10.1016/j.actamat.2020.116546](https://doi.org/10.1016/j.actamat.2020.116546).

## References

- [1] R.O. Ritchie, The conflicts between strength and toughness, Nat. Mater. 10 (2011) 817–822, doi:[10.1038/nmat3115](https://doi.org/10.1038/nmat3115).
- [2] K. Lu, Making strong nanomaterials ductile with gradients, Science 345 (2014) 1455–1456, doi:[10.1126/science.1255940](https://doi.org/10.1126/science.1255940).
- [3] R. Kapoor, Severe plastic deformation of materials, in: A.K. Tyagi, S. Banerjee (Eds.), Materials Under Extreme Conditions, Elsevier, Amsterdam, 2017, pp. 717–754, doi:[10.1016/B978-0-12-801300-7.00020-6](https://doi.org/10.1016/B978-0-12-801300-7.00020-6).
- [4] R.Z. Valiev, R.K. Islamgaliev, I.V. Alexandrov, Bulk nanostructured materials from severe plastic deformation, Prog. Mater. Sci. 45 (2000) 103–189, doi:[10.1016/S0079-6425\(99\)00007-9](https://doi.org/10.1016/S0079-6425(99)00007-9).
- [5] G.S. Dyakonov, S. Mironov, I.P. Semenova, R.Z. Valiev, Strengthening mechanisms and super-strength of severely deformed titanium, in: H. Garbacz, I.P. Semenova, S. Zherebtsov, M. Motyka (Eds.), Nanocrystalline Titanium, Elsevier, Amsterdam, 2019, pp. 123–143, doi:[10.1016/B978-0-12-814599-9.00007-9](https://doi.org/10.1016/B978-0-12-814599-9.00007-9).
- [6] M. Huang, C. Xu, G.H. Fan, E. Maawad, W.M. Gan, L. Geng, F.X. Lin, G.Z. Tang, H. Wu, Y. Du, D.Y. Li, K.S. Miao, T.T. Zhang, X.S. Yang, Y.P. Xia, G.J. Cao, H.J. Kang, T.M. Wang, T.Q. Xiao, H.L. Xie, Role of layered structure in ductility improvement of layered Ti-Al metal composite, Acta Mater. 153 (2018) 235–249, doi:[10.1016/j.actamat.2018.05.005](https://doi.org/10.1016/j.actamat.2018.05.005).

- [7] H. Wu, G.H. Fan, M. Huang, L. Geng, X.P. Cui, H.L. Xie, Deformation behavior of brittle/ductile multilayered composites under interface constraint effect, *Int. J. Plast.* 89 (2017) 96–109, doi:[10.1016/j.ijplas.2016.11.005](https://doi.org/10.1016/j.ijplas.2016.11.005).
- [8] X.L. Ma, C.X. Huang, J. Moering, M. Ruppert, H.W. Höppel, M. Göken, J. Narayan, Y.T. Zhu, Mechanical properties of copper/bronze laminates: Role of interfaces, *Acta Mater.* 116 (2016) 43–52, doi:[10.1016/j.actamat.2016.06.023](https://doi.org/10.1016/j.actamat.2016.06.023).
- [9] X.L. Wu, M.X. Yang, F.P. Yuan, G.L. Wu, Y.J. Wei, X.X. Huang, Y.T. Zhu, Heterogeneous lamella structure unites ultrafine-grain strength with coarse-grain ductility, *Proc. Natl. Acad. Sci. USA* 112 (2015) 14501–14505, doi:[10.1073/pnas.1517193112](https://doi.org/10.1073/pnas.1517193112).
- [10] H.S. Liu, B. Zhang, G.P. Zhang, Enhanced toughness and fatigue strength of cold roll bonded Cu/Cu laminated composites with mechanical contrast, *Scripta Mater.* 65 (2011) 891–894, doi:[10.1016/j.scriptamat.2011.08.001](https://doi.org/10.1016/j.scriptamat.2011.08.001).
- [11] X.T. Fang, G.Z. He, C. Zheng, X.L. Ma, D. Kaoumi, Y.S. Li, Y.T. Zhu, Effect of heterostructure and hetero-deformation induced hardening on the strength and ductility of brass, *Acta Mater.* 186 (2020) 644–655, doi:[10.1016/j.actamat.2020.01.037](https://doi.org/10.1016/j.actamat.2020.01.037).
- [12] Z. Cheng, H.F. Zhou, Q.H. Lu, H.J. Gao, L. Lu, Extra strengthening and work hardening in gradient nanotwinned metals, *Science* 362 (2018) 1925, doi:[10.1126/science.aau1925](https://doi.org/10.1126/science.aau1925).
- [13] G. Dehm, B.N. Jaya, R. Raghavan, C. Kirchlechner, Overview on micro- and nanomechanical testing: new insights in interface plasticity and fracture at small length scales, *Acta Mater.* 142 (2018) 248–282, doi:[10.1016/j.actamat.2017.06.019](https://doi.org/10.1016/j.actamat.2017.06.019).
- [14] Y. Saito, H. Utsunomiya, N. Tsuji, T. Sakai, Novel ultra-high straining process for bulk materials—development of the accumulative roll-bonding (ARB) process, *Acta Mater.* 47 (1999) 579–583, doi:[10.1016/S1359-6454\(98\)00365-6](https://doi.org/10.1016/S1359-6454(98)00365-6).
- [15] M. Ruppert, C. Schunk, D. Hausmann, H.W. Höppel, M. Göken, Global and local strain rate sensitivity of bimodal Al-laminates produced by accumulative roll bonding, *Acta Mater.* 103 (2016) 643–650, doi:[10.1016/j.actamat.2015.11.009](https://doi.org/10.1016/j.actamat.2015.11.009).
- [16] J.T. Avallone, T.J. Nizolek, B.B. Bales, T.M. Pollock, Creep resistance of bulk copper-niobium composites: an inverse effect of multilayer length scale, *Acta Mater.* 176 (2019) 189–198, doi:[10.1016/j.actamat.2019.06.029](https://doi.org/10.1016/j.actamat.2019.06.029).
- [17] T.J. Nizolek, M.R. Begley, R.J. McCabe, J.T. Avallone, N.A. Mara, I.J. Beyerlein, T.M. Pollock, Strain fields induced by kink band propagation in Cu-Nb nanolaminate composites, *Acta Mater.* 133 (2017) 303–315, doi:[10.1016/j.actamat.2017.04.050](https://doi.org/10.1016/j.actamat.2017.04.050).
- [18] L.F. Zeng, R. Gao, Q.F. Fang, X.P. Wang, Z.M. Xie, S. Miao, T. Hao, T. Zhang, High strength and thermal stability of bulk Cu/Ta nanolamellar multilayers fabricated by cross accumulative roll bonding, *Acta Mater.* 110 (2016) 341–351, doi:[10.1016/j.actamat.2016.03.034](https://doi.org/10.1016/j.actamat.2016.03.034).
- [19] J.Q. Duan, M.Z. Qadir, W. Xu, C. Kong, M. Ferry, Texture balancing in a fcc/bcc multilayered composite produced by accumulative roll bonding, *Acta Mater.* 123 (2017) 11–23, doi:[10.1016/j.actamat.2016.10.023](https://doi.org/10.1016/j.actamat.2016.10.023).
- [20] M. Ardeljan, D.J. Savage, A. Kumar, I.J. Beyerlein, M. Knezevic, The plasticity of highly oriented nano-layered Zr/Nb composites, *Acta Mater.* 115 (2016) 189–203, doi:[10.1016/j.actamat.2016.05.058](https://doi.org/10.1016/j.actamat.2016.05.058).
- [21] J.S. Carpenter, T. Nizolek, R.J. McCabe, M. Knezevic, S.J. Zheng, B.P. Eftink, J.E. Scott, S.C. Vogel, T.M. Pollock, N.A. Mara, I.J. Beyerlein, Bulk texture evolution of nanolamellar Zr–Nb composites processed via accumulative roll bonding, *Acta Mater.* 92 (2015) 97–108, doi:[10.1016/j.actamat.2015.03.020](https://doi.org/10.1016/j.actamat.2015.03.020).
- [22] M. Ardeljan, M. Knezevic, T. Nizolek, I.J. Beyerlein, N.A. Mara, T.M. Pollock, A study of microstructure-driven strain localizations in two-phase polycrystalline HCP/BCC composites using a multi-scale model, *Int. J. Plast.* 74 (2015) 35–57, doi:[10.1016/j.ijplas.2015.06.003](https://doi.org/10.1016/j.ijplas.2015.06.003).
- [23] D.J. Savage, I.J. Beyerlein, N.A. Mara, S.C. Vogel, R.J. McCabe, M. Knezevic, Microstructure and texture evolution in Mg/Nb layered materials made by accumulative roll bonding, *Int. J. Plast.* 125 (2020) 1–26, doi:[10.1016/j.ijplas.2019.08.015](https://doi.org/10.1016/j.ijplas.2019.08.015).
- [24] J.G. Kim, S.M. Baek, H.H. Lee, K.-G. Chin, S. Lee, H.S. Kim, Suppressed deformation instability in the twinning-induced plasticity steel-cored three-layer steel sheet, *Acta Mater.* 147 (2018) 304–312, doi:[10.1016/j.actamat.2018.01.042](https://doi.org/10.1016/j.actamat.2018.01.042).
- [25] J.G. Kim, J.W. Bae, J.M. Park, W. Woo, S. Harjo, K.-G. Chin, S. Lee, H.S. Kim, Synergetic strengthening of layered steel sheet investigated using an in situ neutron diffraction tensile test, *Sci. Rep.* 9 (2019) 6829, doi:[10.1038/s41598-019-43369-2](https://doi.org/10.1038/s41598-019-43369-2).
- [26] M. Ojima, J. Inoue, S. Nambu, P. Xu, K. Akita, H. Suzuki, T. Koseki, Stress partitioning behavior of multilayered steels during tensile deformation measured by in situ neutron diffraction, *Scripta Mater.* 66 (2012) 139–142, doi:[10.1016/j.scriptamat.2011.10.018](https://doi.org/10.1016/j.scriptamat.2011.10.018).
- [27] I.A. Ovid'ko, R.Z. Valiev, Y.T. Zhu, Review on superior strength and enhanced ductility of metallic nanomaterials, *Prog. Mater. Sci.* 94 (2018) 462–540, doi:[10.1016/j.pmatsci.2018.02.002](https://doi.org/10.1016/j.pmatsci.2018.02.002).
- [28] Y.P. Li, G.P. Zhang, On plasticity and fracture of nanostructured Cu/X (X=Au, Cr) multilayers: the effects of length scale and interface/boundary, *Acta Mater.* 58 (2010) 3877–3887, doi:[10.1016/j.actamat.2010.03.042](https://doi.org/10.1016/j.actamat.2010.03.042).
- [29] N. Jia, D. Raabe, X. Zhao, Crystal plasticity modeling of size effects in rolled multilayered Cu-Nb composites, *Acta Mater.* 111 (2016) 116–128, doi:[10.1016/j.actamat.2016.03.055](https://doi.org/10.1016/j.actamat.2016.03.055).
- [30] S.J. Zheng, J. Wang, J.S. Carpenter, W.M. Mook, P.O. Dickerson, N.A. Mara, I.J. Beyerlein, Plastic instability mechanisms in bimetallic nanolayered composites, *Acta Mater.* 79 (2014) 282–291, doi:[10.1016/j.actamat.2014.07.017](https://doi.org/10.1016/j.actamat.2014.07.017).
- [31] M. Callisti, T. Polcar, Combined size and texture-dependent deformation and strengthening mechanisms in Zr/Nb nano-multilayers, *Acta Mater.* 124 (2017) 247–260, doi:[10.1016/j.actamat.2016.11.007](https://doi.org/10.1016/j.actamat.2016.11.007).
- [32] Y.Q. Wang, J.Y. Zhang, X.Q. Liang, K. Wu, G. Liu, J. Sun, Size- and constituent-dependent deformation mechanisms and strain rate sensitivity in nanolaminated crystalline Cu/amorphous Cu–Zr films, *Acta Mater.* 95 (2015) 132–144, doi:[10.1016/j.actamat.2015.05.007](https://doi.org/10.1016/j.actamat.2015.05.007).
- [33] T.J. Chen, R. Yuan, I.J. Beyerlein, C.Z. Zhou, Predicting the size scaling in strength of nanolayered materials by a discrete slip crystal plasticity model, *Int. J. Plast.* 124 (2020) 247–260, doi:[10.1016/j.ijplas.2019.08.016](https://doi.org/10.1016/j.ijplas.2019.08.016).
- [34] J.J. Niu, J.Y. Zhang, G. Liu, P. Zhang, S.Y. Lei, G.J. Zhang, J. Sun, Size-dependent deformation mechanisms and strain-rate sensitivity in nanostructured Cu/X (X=Cr, Zr) multilayer films, *Acta Mater.* 60 (2012) 3677–3689, doi:[10.1016/j.actamat.2012.03.052](https://doi.org/10.1016/j.actamat.2012.03.052).
- [35] J.Y. Zhang, K. Wu, L.Y. Zhang, Y.Q. Wang, G. Liu, J. Sun, Unraveling the correlation between Hall-Petch slope and peak hardness in metallic nanolaminates, *Int. J. Plast.* 96 (2017) 120–134, doi:[10.1016/j.ijplas.2017.04.020](https://doi.org/10.1016/j.ijplas.2017.04.020).
- [36] Q.Y. Guo, G.B. Thompson, Evolution of in situ growth stresses and interfacial structure in phase changing Cu/V multilayered thin films, *Acta Mater.* 148 (2018) 63–71, doi:[10.1016/j.actamat.2018.01.023](https://doi.org/10.1016/j.actamat.2018.01.023).
- [37] X.G. Li, L.F. Cao, J.Y. Zhang, J. Li, J.T. Zhao, X.B. Feng, Y.Q. Wang, K. Wu, P. Zhang, G. Liu, J. Sun, Tuning the microstructure and mechanical properties of magnetron sputtered Cu-Cr thin films: the optimal Cr addition, *Acta Mater.* 151 (2018) 87–99, doi:[10.1016/j.actamat.2018.03.044](https://doi.org/10.1016/j.actamat.2018.03.044).
- [38] J.Y. Zhang, J.T. Zhao, X.G. Li, Y.Q. Wang, K. Wu, G. Liu, J. Sun, Alloying effects on the microstructure and mechanical properties of nanocrystalline Cu-based alloyed thin films Miscible Cu-Ti vs immiscible Cu-Mo, *Acta Mater.* 143 (2018) 55–66, doi:[10.1016/j.actamat.2017.09.039](https://doi.org/10.1016/j.actamat.2017.09.039).
- [39] S.J. Zheng, I.J. Beyerlein, J.S. Carpenter, K. Kang, J. Wang, W.Z. Han, N.A. Mara, High-strength and thermally stable bulk nanolayered composites due to twin-induced interfaces, *Nat. Commun.* 4 (2013) 1696, doi:[10.1038/ncomms2651](https://doi.org/10.1038/ncomms2651).
- [40] J.Y. Zhang, X. Zhang, R.H. Wang, S.Y. Lei, P. Zhang, J.J. Niu, G. Liu, G.J. Zhang, J. Sun, Length-scale-dependent deformation and fracture behavior of Cu/X (X=Nb, Zr) multilayers: the constraining effects of the ductile phase on the brittle phase, *Acta Mater.* 59 (2011) 7368–7379, doi:[10.1016/j.actamat.2011.08.016](https://doi.org/10.1016/j.actamat.2011.08.016).
- [41] R. Béjaud, J. Durinck, S. Brochard, Twin-interface interactions in nanostructured Cu/Ag: molecular dynamics study, *Acta Mater.* 144 (2018) 314–324, doi:[10.1016/j.actamat.2017.10.036](https://doi.org/10.1016/j.actamat.2017.10.036).
- [42] Y.X. Zhu, Z.H. Li, M.S. Huang, Y. Liu, Strengthening mechanisms of the nanolayered polycrystalline metallic multilayers assisted by twins, *Int. J. Plast.* 72 (2015) 168–184, doi:[10.1016/j.ijplas.2015.05.014](https://doi.org/10.1016/j.ijplas.2015.05.014).
- [43] J. Wang, R.F. Zhang, C.Z. Zhou, I.J. Beyerlein, A. Misra, Interface dislocation patterns and dislocation nucleation in face-centered-cubic and body-centered-cubic bicrystal interfaces, *Int. J. Plast.* 53 (2014) 40–55, doi:[10.1016/j.ijplas.2013.07.002](https://doi.org/10.1016/j.ijplas.2013.07.002).
- [44] A. Takeuchi, A. Inoue, Classification of bulk metallic glasses by atomic size difference, heat of mixing and period of constituent elements and its application to characterization of the main alloying element, *Mater. Trans.* 46 (2005) 2817–2829, doi:[10.2320/matertrans.46.2817](https://doi.org/10.2320/matertrans.46.2817).
- [45] S. Jiang, R.L. Peng, N. Jia, X. Zhao, L. Zuo, Microstructural and textural evolutions in multilayered Ti/Cu composites processed by accumulative roll bonding, *J. Mater. Sci. Technol.* 35 (2019) 1165–1174, doi:[10.1016/j.jmst.2018.12.018](https://doi.org/10.1016/j.jmst.2018.12.018).
- [46] R. Hielscher, H. Schaeben, A novel pole figure inversion method: specification of the MTEX algorithm, *J. Appl. Cryst.* 41 (2008) 1024–1037, doi:[10.1107/S0021889808030112](https://doi.org/10.1107/S0021889808030112).
- [47] G. Ashiotis, A. Deschildre, Z. Nawaz, J.P. Wright, D. Karkoulis, F.E. Picca, J. Kieffer, The fast azimuthal integration Python library: pyFAI, *J. Appl. Cryst.* 48 (2015) 510–519, doi:[10.1107/S1600576715004306](https://doi.org/10.1107/S1600576715004306).
- [48] T. Gnäupel-Herold, ISODEC: software for calculating diffraction elastic constants, *J. Appl. Cryst.* 45 (2012) 573–574, doi:[10.1107/S0021889812014252](https://doi.org/10.1107/S0021889812014252).
- [49] T. Ungár, I. Dragomir, Á. Révész, A. Borbély, The contrast factors of dislocations in cubic crystals the dislocation model of strain anisotropy in practice, *J. Appl. Cryst.* 32 (1999) 992–1002, doi:[10.1107/S0021889899009334](https://doi.org/10.1107/S0021889899009334).
- [50] T. Ungár, J. Gubicza, G. Ribárik, A. Borbély, Crystallite size distribution and dislocation structure determined by diffraction profile analysis: principles and practical application to cubic and hexagonal crystals, *J. Appl. Cryst.* 34 (2001) 298–310, doi:[10.1107/S0021889801003715](https://doi.org/10.1107/S0021889801003715).
- [51] G. Ribárik, J. Gubicza, T. Ungár, Correlation between strength and microstructure of ball-milled Al–Mg alloys determined by X-ray diffraction, *Mater. Sci. Eng. A* 387–389 (2004) 343–347, doi:[10.1016/j.msea.2004.01.089](https://doi.org/10.1016/j.msea.2004.01.089).
- [52] N. Jia, F. Roters, P. Eisenlohr, D. Raabe, X. Zhao, Simulation of shear banding in heterophase co-deformation: example of plane strain compressed Cu–Ag and Cu–Nb metal matrix composites, *Acta Mater.* 61 (2013) 4591–4606, doi:[10.1016/j.actamat.2013.04.029](https://doi.org/10.1016/j.actamat.2013.04.029).
- [53] S.-B. Lee, J.E. LeDonne, S.C.V. Lim, I.J. Beyerlein, A.D. Rollett, The heterophase interface character distribution of physical vapor-deposited and accumulative roll-bonded Cu–Nb multilayer composites, *Acta Mater.* 60 (2012) 1747–1761, doi:[10.1016/j.actamat.2011.12.007](https://doi.org/10.1016/j.actamat.2011.12.007).
- [54] T. Nizolek, I.J. Beyerlein, N.A. Mara, J.T. Avallone, T.M. Pollock, Tensile behavior and flow stress anisotropy of accumulative roll bonded Cu–Nb nanolaminates, *Appl. Phys. Lett.* 108 (2016) 051903, doi:[10.1063/1.4941043](https://doi.org/10.1063/1.4941043).
- [55] D.K. Yang, P. Cizek, P. Hodgson, C.E. Wen, Ultrafine equiaxed-grain Ti/Al composite produced by accumulative roll bonding, *Scripta Mater.* 62 (2010) 321–324, doi:[10.1016/j.scriptamat.2009.11.036](https://doi.org/10.1016/j.scriptamat.2009.11.036).
- [56] S. Ohsaki, S. Kato, N. Tsuji, T. Ohkubo, K. Hono, Bulk mechanical alloying of Cu–Ag and Cu/Zr two-phase microstructures by accumulative roll-bonding process, *Acta Mater.* 55 (2007) 2885–2895, doi:[10.1016/j.actamat.2006.12.027](https://doi.org/10.1016/j.actamat.2006.12.027).

- [57] L. Ghalandari, M.M. Mahdavian, M. Reihanian, Microstructure evolution and mechanical properties of Cu/Zn multilayer processed by accumulative roll bonding (ARB), *Mater. Sci. Eng. A* 593 (2014) 145–152, doi:[10.1016/j.msea.2013.11.026](https://doi.org/10.1016/j.msea.2013.11.026).
- [58] L. Jiang, M.T. Pérez-Prado, P.A. Gruber, E. Arzt, O.A. Ruano, M.E. Kassner, Texture, microstructure and mechanical properties of equiaxed ultrafine-grained Zr fabricated by accumulative roll bonding, *Acta Mater.* 56 (2008) 1228–1242, doi:[10.1016/j.actamat.2007.11.017](https://doi.org/10.1016/j.actamat.2007.11.017).
- [59] M.J. Hÿtch, J.-L. Putaux, J.-M. Pénisson, Measurement of the displacement field of dislocations to 0.03 Å by electron microscopy, *Nature* 423 (2003) 270–273, doi:[10.1038/nature01638](https://doi.org/10.1038/nature01638).
- [60] Y.N. Wang, J.C. Huang, Texture analysis in hexagonal materials, *Mater. Chem. Phys.* 81 (2003) 11–26, doi:[10.1016/S0254-0584\(03\)00168-8](https://doi.org/10.1016/S0254-0584(03)00168-8).
- [61] M. Knezevic, T. Nizolek, M. Ardeljan, I.J. Beyerlein, N.A. Mara, T.M. Pollock, Texture evolution in two-phase Zr/Nb lamellar composites during accumulative roll bonding, *Int. J. Plast.* 57 (2014) 16–28, doi:[10.1016/j.ijplas.2014.01.008](https://doi.org/10.1016/j.ijplas.2014.01.008).
- [62] J.S. Carpenter, S.C. Vogel, J.E. LeDonne, D.L. Hammon, I.J. Beyerlein, N.A. Mara, Bulk texture evolution of Cu–Nb nanolamellar composites during accumulative roll bonding, *Acta Mater.* 60 (2012) 1576–1586, doi:[10.1016/j.actamat.2011.11.045](https://doi.org/10.1016/j.actamat.2011.11.045).
- [63] A. Fattah-Alhosseini, A.R. Ansari, Y. Mazaheri, M. Karimi, M. Haghshenas, An investigation of mechanical properties in accumulative roll bonded nano-grained pure titanium, *Mater. Sci. Eng. A* 688 (2017) 218–224, doi:[10.1016/j.msea.2017.02.013](https://doi.org/10.1016/j.msea.2017.02.013).
- [64] J.L. Milner, F. Abu-Farha, C. Bunget, T. Kurfess, V.H. Hammond, Grain refinement and mechanical properties of CP-Ti processed by warm accumulative roll bonding, *Mater. Sci. Eng. A* 561 (2013) 109–117, doi:[10.1016/j.msea.2012.10.081](https://doi.org/10.1016/j.msea.2012.10.081).
- [65] H.L. Yu, M. Yan, J.T. Li, A. Godbole, C. Lu, K. Tieu, H.J. Li, C. Kong, Mechanical properties and microstructure of a Ti-6Al-4V alloy subjected to cold rolling, asymmetric rolling and asymmetric cryorolling, *Mater. Sci. Eng. A* 710 (2018) 10–16, doi:[10.1016/j.msea.2017.10.075](https://doi.org/10.1016/j.msea.2017.10.075).
- [66] *Standard Practice for X-ray Determination of Retained Austenite in Steel with Near Random Crystallographic Orientation*, American Society for Testing and Materials, 2013.
- [67] H. Wang, P.D. Wu, J. Wang, C.N. Tomé, A crystal plasticity model for hexagonal close packed (HCP) crystals including twinning and de-twinning mechanisms, *Int. J. Plast.* 49 (2013) 36–52, doi:[10.1016/j.ijplas.2013.02.016](https://doi.org/10.1016/j.ijplas.2013.02.016).
- [68] D.C. Zhang, L.Y. Wang, H. Zhang, A. Maldar, G.M. Zhu, W. Chen, J.-S. Park, J. Wang, X.Q. Zeng, Effect of heat treatment on the tensile behavior of selective laser melted Ti-6Al-4V by in situ X-ray characterization, *Acta Mater.* 189 (2020) 93–104, doi:[10.1016/j.actamat.2020.03.003](https://doi.org/10.1016/j.actamat.2020.03.003).
- [69] M.E. Fitzpatrick, A. Lodini, *Analysis of Residual Stress by Diffraction Using Neutron and Synchrotron Radiation*, first ed., CRC Press, London, 2003.
- [70] P. Ghosh, K.S. Kormout, U. Lienert, J. Keckes, R. Pippan, Deformation characteristics of ultrafine grained and nanocrystalline iron and pearlitic steel - an in situ synchrotron investigation, *Acta Mater.* 160 (2018) 22–33, doi:[10.1016/j.actamat.2018.08.036](https://doi.org/10.1016/j.actamat.2018.08.036).
- [71] H. Li, C.J. Boehlert, T.R. Bieler, M.A. Crimp, Analysis of slip activity and heterogeneous deformation in tension and tension-creep of Ti-5Al-2.5Sn (wt %) using in-situ SEM experiments, *Philos. Mag.* 92 (2012) 2923–2946, doi:[10.1080/14786435.2012.682174](https://doi.org/10.1080/14786435.2012.682174).
- [72] T. Ohashi, M. Kawamukai, H. Zbib, A multiscale approach for modeling scale-dependent yield stress in polycrystalline metals, *Int. J. Plast.* 23 (2007) 897–914, doi:[10.1016/j.ijplas.2006.10.002](https://doi.org/10.1016/j.ijplas.2006.10.002).